Applied Catalysis B: Environment and Energy 344 (2024) 123637

Contents lists available at ScienceDirect

Applied Catalysis B: Environment and Energy

journal homepage: www.elsevier.com/locate/apcatb

# Generating silicon-rich AFX zeolite using rigid diquaternary alkylammonium structure directing agent towards stable selective catalytic reduction of $NO_x$ by $NH_3$

Zheru Shi [a,1], Han Sun [b,1], Lei Wang [c,1], Quanzheng Deng [d], Chen-Xin Gong [a], Lu Han [c], Kaixiang Li [e], Wei Deng [f], Yi-An Zhu [a], Zhenguo Li [e,*], Haijun Chen [b,*], Kake Zhu [a,*]

[a] UNILAB, State Key Laboratory of Chemical Engineering, School of Chemical Engineering, East China University of Science and Technology, 130 Meilong Road, Shanghai200237, PR China
[b] Department of Electronics and Tianjin Key Laboratory of Photo-Electronic Thin Film Device and Technology, Nankai University, Tianjin 300071, PR China
[c] School of Chemistry and Molecular Engineering, Nanjing Tech University, South Puzhu Rd. 30, Nanjing 211816, PR China
[d] School of Chemical Science and Engineering, Tongji University, Shanghai 200092, PR China
[e] National Engineering Laboratory for Mobile Source Emission Control Technology, China Automotive Technology & Research Center Co. Ltd, Tianjin 300300, PR China
[f] School of Optoelectronic Materials and Technology, Jianghan University, Wuhan 430056, PR China

ARTICLE INFO

*Keywords:*
**AFX** zeolite
Organic structure directing agents (OSDAs)
Ammonia selective catalytic reduction ($NH_3$-SCR)
Si/Al ratio

ABSTRACT

New synthetic protocols to manipulate Si/Al ratios of small pore zeolites hold promise to find better selective $NO_x$ reduction catalyst using $NH_3$ as reducing agent ($NH_3$-SCR). **AFX** zeolite as $NH_3$-SCR catalyst is currently impeded by the insufficient hydrothermal stability owing to the low Si/Al ratio. In this contribution, we report the synthesis of **AFX** zeolite using N,N-(1,4-phenylenebis(methylene))bis(N,N,N-triethylammonium) as organic structure directing agent (OSDA) to increase the framework Si/Al ratio to 7.8, giving rise to a marked enhancement of hydrothermal stability to withstand hydrothermal aging at 850 °C for up to 10 h. The increase in Si/Al ratio for **AFX** zeolite minimizes catalytic cycle driven by Brønsted acid site and broadens high temperature operation window (150–515 °C) for Cu-exchanged catalyst. Moreover, the hydrothermally aged Cu-AFX catalyst exhibits comparable catalytic activity to that of the fresh catalyst owing to Cu predominant distribution close to the 6-MR.

## 1. Introduction

$NO_x$ (NO or $NO_2$) formed from $N_2$ and $O_2$ during combustion process is unavoidable for lean-burn engines in automobiles, such as diesel engines or stationary sources, like engineering machinery, farming machinery and marine engines. $NO_x$ is an important precursor for the formation of acid rain, photochemical smog and haze, hence, constitutes a major threat to environment, ecology system and human health [1]. The start-of-the-art $NO_x$ selective catalytic reduction using ammonia ($NH_3$-SCR) as reductant is capable of converting $NO_x$ in the presence of excessive $O_2$. For use as $NH_3$-SCR catalyst, low temperature (below 200 °C) activity is desired under cold-start and low-load conditions. Concomitantly, high-temperature (above 650 °C) hydrothermal stability is critical in regeneration environment of the upstream diesel particle filter. As a replacement of toxic transition metal oxides (such as $V_2O_5$-$WO_3$($MoO_3$)/$TiO_2$) catalysts, Cu or Fe-exchanged zeolite catalysts [2], like medium pore Cu-ZSM-5 [3] and large pore Cu-Beta [4], first appeared in the 1980 s, which were later abandoned for their unsatisfactory (hydro)thermal stability, formation of $CuO_x$ and poor poisoning-resistance towards hydrocarbons, alkali metals, $SO_2$ etc. [5]. Thereafter, Cu-exchanged small pore zeolites have been recognized to possess sufficient hydrothermal stability to withstand the harsh $NH_3$-SCR conditions, owing to the stabilization of $Cu^{2+}$ and $Cu(OH)^+$ by the presence of 6-membered ring (6-MR) or 8-MR [6], resulting in the commercialization of Cu-CHA and Cu-AEI as catalysts for $NO_x$ elimination for diesel engine exhaust in 2010 s [7]. These zeolites also show outstanding catalytic efficiency, wide operation temperature window (200–500 °C) and prominent poison resistance. The successful

* Corresponding authors.
*E-mail addresses:* lizhenguo@catarc.ac.cn (Z. Li), chenhj@nankai.edu.cn (H. Chen), kakezhu@ecust.edu.cn (K. Zhu).
[1] These authors contributed equally to this work.

https://doi.org/10.1016/j.apcatb.2023.123637

Available online 19 December 2023
0926-3373/© 2023 Elsevier B.V. All rights reserved.

deployment of Cu-CHA has since then inspired research interest on the exploration of other small pore zeolites [8], such as **AEI** [9,10], **LEV** [11], **AFT** [12], **ERI** [13], **LTA** [14,15], **KFI** [16] and **RTH** [17,18] zeolites as potential $NH_3$-SCR catalysts. Zeolites belonging to both the ABC-6 and double 6-ring (*d6r*) families, including **AFX**, **AFT** and **SFW** [19,20] show promising $NH_3$-SCR catalytic properties in terms of wide temperature window with respect to the commercialized counterpart [21–24], but the Si/Al ratio dependent hydrothermal stability remains a major obstacle. The material design for **AFX** zeolite with enhanced hydrothermal stability, broadened operation temperature window is desirable to the discovery of better candidate $NO_x$ abatement catalyst.

**AFX**-structured zeolite is built up of AABBCCBB sequenced *d6r* and comprises of a large and elongated *aft* ($4^3 4^6 6^2 8^3 8^9$, 5.5 × 13.5 Å) cage and a smaller *gme* ($4^3 4^6 6^2 8^3$, 3.3 × 7.4 Å) cage that are connected by 8-MR openings (3.4 × 3.6 Å), as exhibited in Fig. 1a. **AFX** topology was first discovered in silicoaluminophosphate form (SAPO-56) [25], while the aluminosilicate variant, named SSZ-16, was crystallized using 1, 1'-tetramethylenebis(1-azoniabicyclo[2.2.2]octane) dication dibromide as organic structure-directing agent (OSDA) [26] under highly alkali medium, i.e., high $Na^+$/Si ratio (~1) in the synthesis solution. The obtained material, nevertheless, has low Si/Al ratio (< 6) and consequently unsatisfactory hydrothermal stability for use as $NH_3$-SCR catalyst. Since then, persist synthesis efforts to broad the framework compositions have been undertaken to generate **AFX** zeolite with elevated Si/Al ratios, and several alternative diquaternary OSDAs, such as 1,1´-(1,4-butanediyl) bis(1-azonia-4-azabicyclo[2.2.2]octane) ($[Dab_4]^{2+}$) [27], N,N´-bis--triethylpentanediyldiammonium cation ($Et_6$-diquat-5) [28] etc., have thus far been developed. Martín et al. [21] proposed the rigid OSDA,

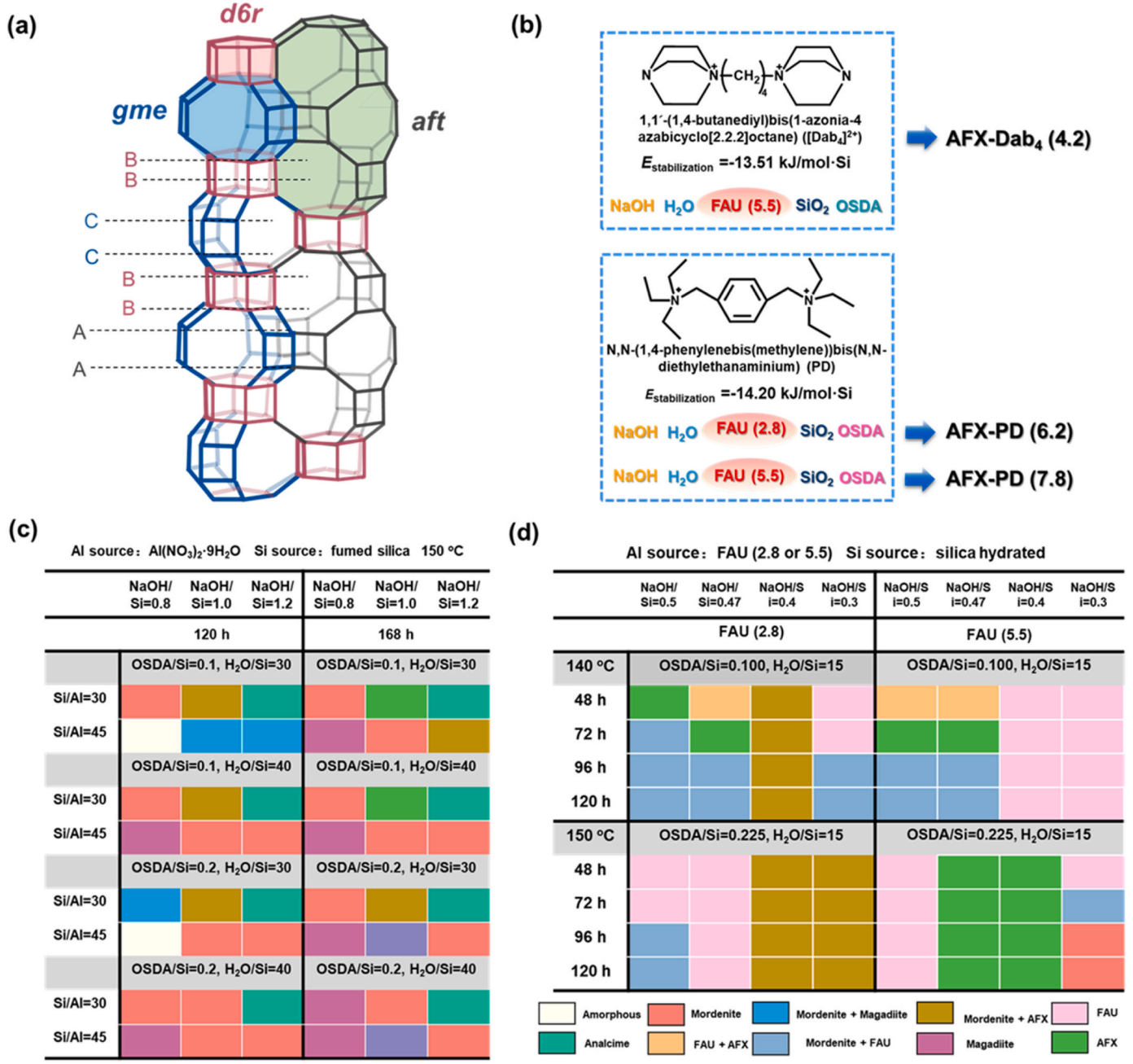


**Fig. 1.** The structure model of **AFX** zeolite, whereby the stacking sequence of *d6r* building units and the *gme*, *aft* cages are highlighted (a). The structure of $Dab_4$, PD and the nomenclature of sample names (b). Exploratory synthetic outcome using conventional inorganic raw materials (c) and two types of **FAU** zeolites (with Si/Al ratios of 2.8 and 5.5) as Al sources crystallized by crystal transformation(d).

combined with inter-zeolite conversion using high silicon zeolite **FAU** (Si/Al= 6, 11, 25) as Si and Al sources, to generate **AFX** (Si/Al= 5.3). Along the route, Han et al. [29] very recently reported N,N′-dimethyl-N,N,N′,N′-tetraethylhexanediyldiammonium as an optional OSDA to crystallize **AFX** zeolite with Si/Al of 6.7. The increase in framework Si/Al ratios for the obtained **AFX** zeolite was found to be marginal (normally between 3.1 and 6.7) using these inexpensive diquaternary OSDAs. In addition, 1,3-bis(1-adamantyl)imidazolium hydroxide as OSDA was proposed by Davis et al. [30] to allow the generation of **AFX** zeolite with a record high Si/Al ratio of 16.7, which, unfortunately, necessities the use of costly raw materials and laborious procedures to prepare the OSDA, making it prohibitively expensive as a practical solution. Kubota et al. [31]developed an **AFX** zeolite using a bulky and non-flexible OSDA named N,N,N,N-tetraethylbicyclo[2.2.2]oct-7-ene-2,3 , 5,6-dipyrrolidinium dication ($TEBOP^{2+}$), for the synthesis of **AFX** with a higher stability than the conventional **AFX**-type zeolite. Sano's [32] group used co-templating strategy, tetramethylammonium ($Me_4N^+$) and $TEBOP^{2+}$ to fabricate **AFX** zeolite with Si/Al of 7.9. These reported OSDAs, reaction conditions, hydrothermal stability and the Si/Al ratios of the resultant products are compiled in Table S1, in the Supplementary Information (SI). Another drawback of synthesis is that most **AFX** zeolite crystallization is conducted in highly alkali media (high $Na^+$/Si ratio, i.e., 0.8 to 2.4, in the starting gels), which often give rise to low synthesis yields, as a significant amount of the precursors remain in the supernatant solution. From these pioneering investigations, it is instructive to learn that the discovery of more effective, bulky and rigid OSDAs and high silicon **FAU**-to-**AFX** inter-zeolite conversion are the two primary synthetic strategies. As high silicon **FAU** (Si/Al > 6) zeolite cannot be directly synthesized using simple inorganic raw materials, their preparations often involve complicated post-synthetic processes. In brief, the genuine challenge for **AFX** zeolite synthesis for use as $NH_3$-SCR catalyst is to pinpoint a low-cost OSDA and appropriate crystallization conditions to elevate the framework Si/Al ratio between 6 and 16 using inexpensive precursors, for which a solution remains yet unresolved.

The increase of Si/Al ratio for small pore zeolites is pivotal for their acidity, tolerance to poisonings, catalytic activity, hydrothermal stability as a $NH_3$-SCR catalyst. On one hand, the Al content and configuration (single Al or paired Al sites) govern the nature and concentration of exchangeable copper ($Cu^{2+}$-2Al, $[Cu(OH)]^+$-Al) and proton sites, which can critically impact for the low temperature activity driven by $NH_3$–solved copper dimer ($Cu(NH_3)_2$-$O_2$-$Cu(NH_3)_2$) mechanism [33]. Dynamic formation of copper dimer is regarded as the rate-determining step for the low temperature (~150–250 °C) regime of $NH_3$–SCR, which are dependent on factors such as framework Si/Al ratio [34], Cu content [35] and zeolite topology [36,37]. In the high temperature regime, single copper sites are considered to be the active sites, for which excessive loading may cause sluggish NO reduction as a consequence of $NH_3$ oxidation by $O_2$ [38]. Besides, formation of ammonium nitrate is favored on aluminous zeolites or at elevated copper loadings, which may block pore entrance for reactants and decompose into chemically less reactive $N_2O$ [39]. On the other hand, the hydrothermal stability is highly dependent on framework Al content and configurations, as well as the nature and concentrations of copper cations. As the probability of forming paired sites (-Al-O-Si-O-Al- bond) increases on aluminous samples and hydrothermal aging process selectively removes these paired Al sites, the increase in framework Si/Al ratio can boost the hydrothermal stability by avoiding formation of such moieties [40]. While $Cu^{2+}$ cation can boost the hydrothermal stability by stabilizing the 6-MR, $CuO_x$ clusters may accumulate and react with hydrolyzed framework Al over aluminous sample to afford $CuAl_2O_4$, a process that causes zeolite framework collapse [41]. Indeed, the Cu-CHA catalyst only becomes a practical catalyst after the silicon-rich variant of chabazite becomes synthesizable using N,N,N-trimethyl-1-adamantam monium hydroxide as OSDA [42]. Likewise, the identification of 1,2-dimethyl-3-(4-methyl-benzyl)-imidazolium and tetramethylammonium as an OSDA has enabled the use of synthetic Si-rich **LTA** zeolite (Si/Al ca. 16–23), whose Al-rich variant is only applicable as sorbents or ion-exchangers for the low stability, to be a more stable SCR catalyst than that of SSZ-13 [43]. Hence, the ability to regulate Si/Al ratio lay the basis to enhance robustness of working catalyst.

In this work, we investigate the use of N,N-(1,4-phenylenebis(methylene))bis(N,N,N-triethylammonium) (PD) as OSDA for the generation of silicon-rich **AFX** zeolite and the catalytic consequence in $NH_3$-SCR reaction. Zones and co-workers [44,45] demonstrated that OSDAs with an intermediate $C/N^+$ ratio (between 11 and 16) have the highest tendency to crystallize high-silica zeolites, as they are soluble in water and sufficiently hydrophobic such that there is a preferred attraction to the silicate species over water. PD was designed as it mimics in structure to the previously reported $Et_6$-diquat-5 ($C/N^+$= 8), but has a high $C/N^+$ ratio of 10 and a rigid linker between quaternary cations. It is postulated that the both factors can lower the charge density of the OSDA and consequently increase the Si/Al ratio (equivalent to lower the charge density) of the inorganic framework, since charge density match has been recognized as a determinant factor for zeolite crystallization and a means to regulate framework compositions[46,47]. The influence of synthesis factors, including additional chemical (e.g., heteroatoms, inorganic cations, seeds) and physical (e.g., temperature, time, agitation) factors affect the Si/Al ratios of products, have been extensively screened. The use of inexpensive **FAU** zeolite (Si/Al of 2.8 and 5.5) as Al source under optimized crystallization conditions produces **AFX** zeolite with Si/Al ratios of 6.2 and 7.8 in high yields. This widening of compositions has enabled the material to withstand hydrothermal treatment at harsh temperature of 850 °C, under which the control sample has collapsed, thus exhibiting comparable hydrothermal stability to these of commercially used ones. Since Brønsted acid sites (BAS) alone [48] or in junction with Cu sites can function as active sites for $NO_x$ reduction, the tuning of framework compositions also allows the discrimination of their respective contributions to be inspected at varied temperatures, over both proton-type and Cu-AFX catalysts. BAS driven mechanism is found to diminish, while Cu-sites triggered reaction appear unaffected, with increasing Si/Al ratio. A broad activity temperature window ranging from ~150 to 515 °C is achieved for Cu-AFX zeolite, outperforming reported Cu-CHA catalyst in the high temperature region. Moreover, the high activity is preserved after hydrothermal aging for the silicon-rich Cu-AFX catalyst, owing to the increase of framework Si/Al ratio and predominant distribution of Cu cations on sites close to 6-MR.

## 2. Experimental section

### 2.1. Synthesis of the OSDAs

The used OSDA N,N-(1,4-phenylenebis(methylene))bis(N,N,N-triethylammonium)$(OH)_2$ (abbreviated as $PD(OH)_2$) was synthesized as follows: 36.70 mmol of 1,4-bis(bromomethyl)benzene (97%, TCI) and 73.40 mmol of triethylamine were dissolved in 500.00 mL of ethanol, and the resultant solution was refluxed at 70 °C for 72 h. Afterwards, the solvent was removed using a rotary evaporator and the solid precipitate was recrystallization in 300.00 mL acetone, dried in vacuum to give the dibromide product yield 98%. The resultant bromide salt was ion-exchanged to the hydroxide from using Anionic 717 resin. The typical mass ratio employed for the ion-exchange was 1:3:5 for dibromide product: resins: water at room temperature for 12 h. Finally, the hydroxide solution was evaporated to afford aqueous solution, with an overall yield of ca. 90%, as confirmed by titration measurements.

The conventionally used OSDA $[Dab_4]^{2+}(Br^-)_2$, was synthesized as follows: 450.00 mmol of 1,4-Diazabicyclo [2.2.2] octane (DABCO; 51.50 g, Aldrich) was dissolved in 400.00 mL of acetone and 80.30 mmol of 1,4-dibromobutane (17.70 g, Wako) was added slowly at room temperature for a period of 15 min. Another 80.00 mL of acetone was added and the whole mixture was stirred for 48 h. The resultant white suspension was filtered and the white solid was collected, washed successively with acetone, and subsequently dried in vacuo to give the

dibromide salt product, with a yield 99%. The hydroxide form $[Dab_4]^{2+}(OH^-)_2$ was obtained after ion-exchange procedures, as described above.

#### 2.1.1. Synthesis of AFX-type zeolite using PD

**AFX** zeolite was synthesized from a gel with molar composition of 1.00 $SiO_2$: 0.028 $Al_2O_3$: 0.40 NaOH: 0.225 $PD(OH)_2$: 15 $H_2O$ [49]. In a typical run, $PD(OH)_2$ and sodium hydroxide (96%, TCI) were dissolved in deionized water. A commercial **FAU** zeolite (Si/Al= 2.8 or Si/Al= 5.5, $Na^+$ type, Nankai University) was then added as the Si and Al source. The reaction mixture was vigorously agitated by a planetary centrifugal mixer before being transferred to a Teflon-lined stainless steel autoclave, to proceed at hydrothermal treating 140–150 °C under tumbling (50 rpm) for a duration of 48–144 h. The resultant solid was washed three times with deionized water and ethanol. The obtained solid was dried at 80 °C for 12 h in a convection oven.

As-synthesized Na-AFX materials were calcined at 550 °C in air for 8 h to remove the occluded OSDA. The calcined Na-AFX samples were ion-exchanged three in 1.0 M $NH_4Cl$ solutions at 80 °C for 12 h (1.00 g zeolite per 100.00 mL solution), to produce $NH_4^+$-AFX zeolite. The proton form of H-AFX was prepared by calcination of the $NH_4$-AFX zeolite in muffle oven at 550 °C for 8 h, with a ramp of 2 °C·min$^{-1}$.

#### 2.1.2. Synthesis control AFX zeolite using $[Dab_4]^{2+}$

Control **AFX** zeolite was generated using a modified synthesis method [50]: The molar composition of the synthesis mixture was 1.00 $SiO_2$: 0.033 $Al_2O_3$: 0.09 $[Dab_4]^{2+}(OH^-)_2$: 0.55 NaOH: 20.00 $H_2O$. To generate the sample, 7.20 g of $[Dab_4]^{2+}(OH^-)_2$ aqueous solution and 1.70 g of NaOH solution were dissolved in 30.90 g of deionized water, to which 3.30 g of silica hydrated was added at room temperature. The mixture was stirred to stand statically for 24 h. To the above suspension, 2.20 g of **FAU** seed crystals (SiAl =5.5, HSZ-320HOA, Tosoh Co.) were added and mixed. The synthetic mixture was charged into a Teflon-lined 100 mL stainless steel autoclave and put in a convection oven at 140 °C for 48 h. The solid white powder was recovered by centrifugation and dried at 80 °C for 12 h. The sample was calcined in a muffle furnace with the temperature raised from room temperature to 500 °C with a 2 °C·min$^{-1}$ ramping rate, and maintained at the same temperature for 8 h. Ion-exchange and calcination to form the proton-type zeolite was undertake following the same procedures, as illustrated before.

### 2.2. Cu-exchange procedure

The H-AFX type zeolites were ion-exchanged with an aqueous solution of 0.025 M $Cu(CH_3CO_2)_2$ (95%, TCI), maintaining a solid to liquid ratio of 1:100 at room temperature for 10 h, under vigorous magnetic stirring. Afterwards, the samples were filtered, washed with deionized water and calcined at 550 °C for 6 h with a ramp of 2 °C·min$^{-1}$.

### 2.3. Characterization techniques

Powder X-ray Diffraction (PXRD) patterns were equipped with a D8 Advance (Bruker AXS GmbH, Germany) diffractometer, operating at 40 kV and 100 mA, and using Cu Kα radiation (= 1.5418 Å). The PXRD data for the structural refinement equipped with a Mythen 1 K detector in the Debye–Scherrer geometry (wavelength λ: 0.6887 Å, beam energy: 18 keV, calibrated by NIST standard reference material® 660a) at the Shanghai Synchrotron Radiation Facility (SSRF) on an X-ray diffraction beamline (BL14B1). Before measurements, the as-synthesized zeolite powder was loaded in a 0.5 mm borosilicate glass capillary. The diffraction patterns were collected in a $2\theta$ range of 3–50° with a fixed step size of 0.004° at room temperature. To figure out different guest species occluded in the as-made zeolite, the Rietveld refinement was carried out with a commercial TOPAS V5.0 suite. The sizes and morphological features of the samples were investigated by photo micrographing with Field-Emission Scanning Electron Micrographs (FE-SEM) and Transmission Electron Micrographs (TEM) using a NOVA Nano SEM 450 (FEI, USA) microscope and a JEM-2011 (JEOL) equipment, respectively. The chemical analyses of all samples were carried out in Inductively Coupled Plasma Atomic Emission Spectrometry (ICP-AES) conducted on an IRIS 1000 instrument (Agilent Technologies, USA) and vario EL cube Elemental Analyzer (Elementar, Germany). The Nuclear Magnetic Resonance (NMR) spectra were carried out at room temperature with a Bruker AV 600 MHz spectrometer. $^{27}Al$ MAS NMR spectra were recorded at a frequency of 104.3 MHz with a spinning rate of 12 kHz, 1200 scans, and 0.4 s recycle delay, and calibrated with 1.0 wt% aluminum nitrate ($Al(NO_3)_3$) aqueous solution. $^{29}Si$ MAS NMR spectra were scanned 240 times at a frequency of 79.6 MHz and a spinning rate of 4 kHz with a 15 s recycle delay. Tetramethylsilane was used as the chemical shift reference. The framework $SiO_2/Al_2O_3$ ratio could be calculated using the areas of different Si(nAl) by the following equation [51]:

$$(Si/Al)_{NMR} = \sum I_{Si(nAl)} \Big/ \sum 0.25 n I_{Si(nAl)} \quad (1)$$

The textural characteristics were determined by $N_2$ adsorption-desorption isotherms were measured on an ASAP 2020 (Micromeritics, USA). The powder samples were degassed under vacuum at 350 °C for 24 h in order to remove surface contaminant before collecting the $N_2$ physisorption data at -196 °C. The Brunauer-Emmett-Teller (BET) method was used to determine the surface areas. The Pore volumes and micropore volumes were calculated by Non-Local-Density Functional Theory (NLDFT) and the *t*-plot method, respectively. X-ray Photoelectron Spectroscopy (XPS) was conducted to analysis the oxidation state of Cu element in catalysts (ESCALAB 250Xi, ThermoFisher).

Temperature-Programmed Reduction by hydrogen ($H_2$-TPR) experiments were conducted with a Micromeritics AutoChem II 2920 analyzer. For the analysis, 100.00 mg sample was weighed and placed in a U-shaped quartz tube. The sample was heated at 10 °C·min under 10% $O_2$/He flow from room temperature to 300 °C for 2 h to remove absorbed water before cooling to 50 °C, $H_2$-TPR measurements were recorded in 10% $H_2$/Ar flow (50 mL·min$^{-1}$) with a heating rate of 10 °C·min$^{-1}$ to reach a final temperature of 1000 °C. The consumption of $H_2$ was monitored with a thermal conductivity detector (TCD), which was stabilized for 30 min in a 10% $H_2$/Ar flow (50 mL·min$^{-1}$) before the measurement.

Thermogravimetric Analysis (TGA) was operated on a thermogravimetric analyzer Pyris 1 TGA setup under air atmosphere. All samples were heated to 900 °C from room temperature at a rate of 5 °C·min$^{-1}$. $NH_3$ temperature programmed desorption ($NH_3$-TPD) was used to characterize acid strength by an Auto Chem II chemisorption instrument (Micromeritics Co., USA). The Fourier-transform infrared spectra of adsorbed ammonium ($NH_3$-IR) over **AFX** samples were performed to measure the acidity using a Spectrum 100 Fourier transform infrared spectrometer. The total number of acid sites referring to the molar extinction coefficients of $\varepsilon_{\text{Brønsted}}$ (1450 cm$^{-1}$) = 1.47 cm·μmol$^{-1}$ and $\varepsilon_{\text{Lewis}}$(1630 cm$^{-1}$) = 1.98 cm·μmol$^{-1}$ [52].

In situ FT-IR experiments was recorded on Thermal Scientific Nicolet iS 10 with a DTGS detector. ZnSe windows were used in the transmission cell. ~10 mg of the sample was pressed into slice at 0.8 Mpa with a diameter of 13 mm. The samples were heated at 550 °C in a flow of 50 mL·min$^{-1}$ air for 60 min to remove surface contaminates, before cooling down to 100 °C to collect background baseline under Ar atmosphere (100 mL·min$^{-1}$ for 120 min). The data were overlapped 16 times with a resolution of 4 cm$^{-1}$ in anhydrous environment. The spectra were collected after exposing to 500 ppm $NH_3$ or 500 ppm CO diluted using

He as balance gas (with a flow rate of 100 mL·min$^{-1}$ for 30 min), and the same overlapping was followed.

### 2.4. Molecular modeling

Molecular simulations were applied to compute the stabilization energy between **AFX** framework and OSDA. In this study, we utilized the Forcite module within Materials Studio for tasks such as structural optimization and single-point energy calculations, all employing COMPASS force fields. Crystal structure data of **AFX** zeolite was taken from the International Zeolite Association (www.iza-structure.org). The atomic coordinates of the **AFX** zeolite were fixed, and subsequently, pre-optimized OSDA molecules were manually positioned inside the *aft* cages of **AFX**, with one OSDA molecule placed in each cage. Following this, the frozen pose method was used to determine the stabilization energy. The stabilization energy is defined as the energy difference between AFX_OSDA, AFX framework, and OSDA alone, depicted as following:

$$E_{(\text{stabilizationenergy})} = \left[E_{(AFX_OSDA)} - E_{(AFX)} - nE_{(OSDA)}\right]/N \quad (2)$$

Where $n$ refers to the number of occluded OSDA, while $N$ being the number of T atoms, in one **AFX** unit cell.

### 2.5. Accelerated hydrothermal aging treatments

A severe, accelerated hydrothermal aging of the Cu-containing zeolites was performed by steaming the solids in a tube furnace with a ramp of 1 °C·min$^{-1}$ to 750 °C or 850 °C, soaked at the intended temperature for 750 °C 24 h or 850 °C 10 h in air (mL·min$^{-1}$), and then cooled. The products denoted as CuAFX-PD (6.2 or 7.8)-HT750 and CuAFX-PD (6.2 or 7.8)-HT850, respectively.

### 2.6. Catalytic assessments in $NH_3$-SCR

0.20 g of catalyst (18–30 mesh) was loaded in quartz tube for the catalytic activity test, which was carried out in a fixed-bed reactor with the reactant gas mixture containing 500 ppm NO, 500 ppm $NH_3$, 15% $O_2$ and 5% $H_2O$ in $N_2$ balance. The total gas flow through the catalysts was set to 1667 mL·min$^{-1}$ with a GHSV of 200, 000 $g_{\text{-NO}}\cdot(g_{\text{-cat.}}\cdot h)^{-1}$. The temperature was measured from 100 °C to 600 °C. NO, $NO_2$, and $N_2O$ of outlet gas were quantified by FTIR spectrometer (Thermo Nicolet iS 10). The NOx conversion was calculated based on the formula as following:

$$NO_x\text{conversion} = \left(1 - \frac{[NO_x]_{out}}{[NO_x]_{in}}\right) \times 100\% \left(NO_x = NO + NO_2\right) \quad (3)$$

$$N_2O\text{selectivity} = \left(\frac{2 \times [N_2O]_{out}}{[NO]_{in} + [NH_3]_{in} - [NO]_{\text{out}} - [NH_3]_{out}}\right) \times 100\% \quad (4)$$

## 3. Results and discussion

### 3.1. Exploratory synthesis

From the structure model of **AFX** zeolite, whereby the stacking sequence of *d6r* building units, the *gme* with a BBCC sequence, and *aft* cages with an AABBCCBB sequence are highlighted in Fig. 1a. PD, as shown in Fig. 1b, has been selected as OSDA for the crystallization of **AFX** zeolite because the molecule structurally mimics $Et_6$-diquat-5, the often used one, and the replacement of the flexible methylene chain by aromatic ring would exert rigidity to the molecule. Enhancement of OSDA rigidity is a proven means to widen inorganic framework of zeolitic materials [53,54]. Increase of C/N$^+$ of OSDA often suggests a decrease of its charge density, correspondingly, a decrease of the matching charge density for the zeolitic inorganic framework, which, in turn, translating to an increased Si/Al ratio. We have calculated the stabilization energy of PD to the framework using a siliceous model of **AFX** zeolite by force fields (FFs) method. The stabilization energy normalized to per framework $SiO_4$ was deduced to be − 14.20 kJ·mol$^{-1}$·Si$^{-1}$, which is lower than that of $[Dab_4]^{2+}$ (−13.51 kJ·mol$^{-1}$·Si$^{-1}$), recommending that PD is a better suited OSDA for **AFX** zeolite synthesis.

Exploratory synthesis started with bromide-type PD as OSDA, Al $(NO_3)_2$·9 $H_2O$ and fumed silica as inorganic raw materials. The influences of NaOH/Si ratio (manipulated to be 0.8, 1.0 and 1.2), OSDA/Si ratio (varied to be 0.1 and 0.2), $H_2O$/Si ratio (30 or 40), Si/Al ratio of the initial gel (30 or 45), as well as crystallization period (120 or 168 h) were extensively investigated under typical crystallization conditions, which amounted to a total number of 48 entries, and the synthetic outcomes were compiled in Fig. 1c. In most cases, competing phases, such as mordenite (**MOR**), dense phase analcime (**ANA**) or magadiite were observed to co-exist in the products, likely because of the high alkalinity and $Na^+$ concentrations in the synthesis gel [55]. Within a narrow synthetic window at 150 °C, with a molar compositions of 1.00 $SiO_2$: 0.033 $Al_2O_3$: 1.00 NaOH: 0.10 $PD(Br)_2$: 30–40 $H_2O$, pure phase **AFX** zeolite could be generated, while attempts at lower temperatures failed to produce zeolitic products. Still, the Si/Al ratio of the obtained **AFX** zeolite was only 4.5, and the yield was less than 20%, owing to the high $Na^+$/Si ratios in the starting batches.

Next, investigations were steered towards lowering the $Na^+$/Si ratio of the starting materials, in order to suppress formation of competing phases directed by excessive $Na^+$. To maintain the necessary alkalinity for crystallization, the hydroxide form of OSDA was used instead, such that a high overall $OH^-$/Si ratio could be maintained. In addition, two types of **FAU** zeolites, with Si/Al ratios of 2.8 and 5.5 were employed as Al sources, with the proven benefits of (i) increasing Si/Al ratio of synthetic *d6r* small pore zeolite products (such as **CHA** [56], **AEI** and **AFX** [57]) and (ii) shortening of crystallization time [58]. **FAU** zeolite is considered to depolymerize under hydrothermal conditions and release *d6r* building units that can be readily incorporated into the **AFX** framework [59]. A total number of 64 syntheses were designed, as outlined in Fig. 1d, with respect to controlled NaOH/Si ratio (lowered to 0.50, 0.47, 0.40 and 0.30), Al sources (**FAU** zeolites with Si/Al ratios of 2.8 and 5.5), OSDA/Si ratios (0.100 and 0.225), crystallization durations (48, 72, 96 and 120 h) and two typical crystallization temperatures (140 and 150 °C). The two **FAU** zeolites with relatively low Si/Al ratios were selected for their inexpensiveness. It is seen that replacement of Al source has expanded the synthetic window for pure phase **AFX** zeolite fabrication, especially when **FAU** zeolite with Si/Al of 5.5 is adopted. Starting with a synthetic gel of molar composition 1.00 $SiO_2$: 0.033 $Al_2O_3$: 0.47 NaOH: 0.10 $OSDA(OH)_2$: 15 $H_2O$. First, $PD(OH)_2$, using **FAU** (SiAl = 2.8) as Al source after crystallization at 140 °C for 72 h, typically, highly crystalline sample, herein labeled as AFX-PD (6.2), whereby the suffix indicating Si/Al ratio, could be generated. The use of **FAU** (Si/Al= 5.5) as Al source, with a batch composition of 1.00 $SiO_2$: 0.033 $Al_2O_3$: 0.40 NaOH: 0.225 $PD(OH)_2$: 15 $H_2O$, created a sample named AFX-PD (7.8) after heating at 150 °C for 120 h. The Si/Al ratio for products was determined by ICP-AES. Here, it is noteworthy that the AFX-PD (7.8) sample has thus far the third highest Si/Al ratio of known recipes, while the Si/Al ratios for other high silicon samples were measured solely by Energy Dispersive Spectrometer (EDS), while the framework composition still awaits further validations [21,31]. From Fig. 1c and d, it can be generalized that the increase of Si/Al ratio of precursor synthesis gel, the use of **FAU** zeolite as Al source and lowering the $Na^+$/Si ratios to 0.40 to 0.47, are necessary for the increase of product Si/Al ratio.

At this point, we have identified the optimized recipes for silicon-rich **AFX** zeolites fabrication using $PD(OH)_2$ as OSDA, and further explorations over structural features, hydrothermal stability and catalytic properties are focused on the two typical samples. For comparison, these data for a control sample, denoted as AFX-$Dab_4$(4.2), derived using $[Dab_4]^{2+}(OH^-)_2$ as OSDA, are also included.

### 3.2. Characterizations of Si-rich AFX zeolites

Phase compositions of calcined samples are determined by powder XRD technique, and all diffraction lines from these samples coincide with that of hexagonal *P6₃/mmc* phase (JCPDS No. 47–0763), as exhibited in Fig. 2a, validating the successful crystallization of **AFX** zeolite. The relative crystallinities (RC) are calculated with respect to the control NaAFX-Dab$_4$ sample (whose RC is defined to be 100%). RC are determined to be 108% and 162% for NaAFX-PD (6.2) and NaAFX-PD (7.8), respectively, revealing that PD outperforms $[Dab_4]^{2+}$ as OSDA. Increase of Si/Al ratio has produced **AFX** zeolite with relative high crystallinity, which often implies better (hydro)thermal stability. After indexation, the lattice parameters for each sample can be generated, as outline in Table 1. The measured ***a*** parameters are, respectively, 13.77, 13.65 and 13.52 Å, and the ***c*** values are 19.96, 19.92 and 19.89 Å, for NaAFX-Dab$_4$ (4.2), NaAFX-PD (6.2) and NaAFX-PD (7.8), respectively. Lattice shrinkage has been observed, in particular for ***a*** parameter, as Al-O bond (1.736 Å) is longer than that of Si-O bond (1.603 Å), more substitution of Al atoms by Si would induce lattice reduction [60]. High resolution powder XRD diffraction for as-synthesized sample was also collected using synchrotron radiation as X-ray source, such that Rietveld refinement could be performed. In the beginning, the Pawley fitting was

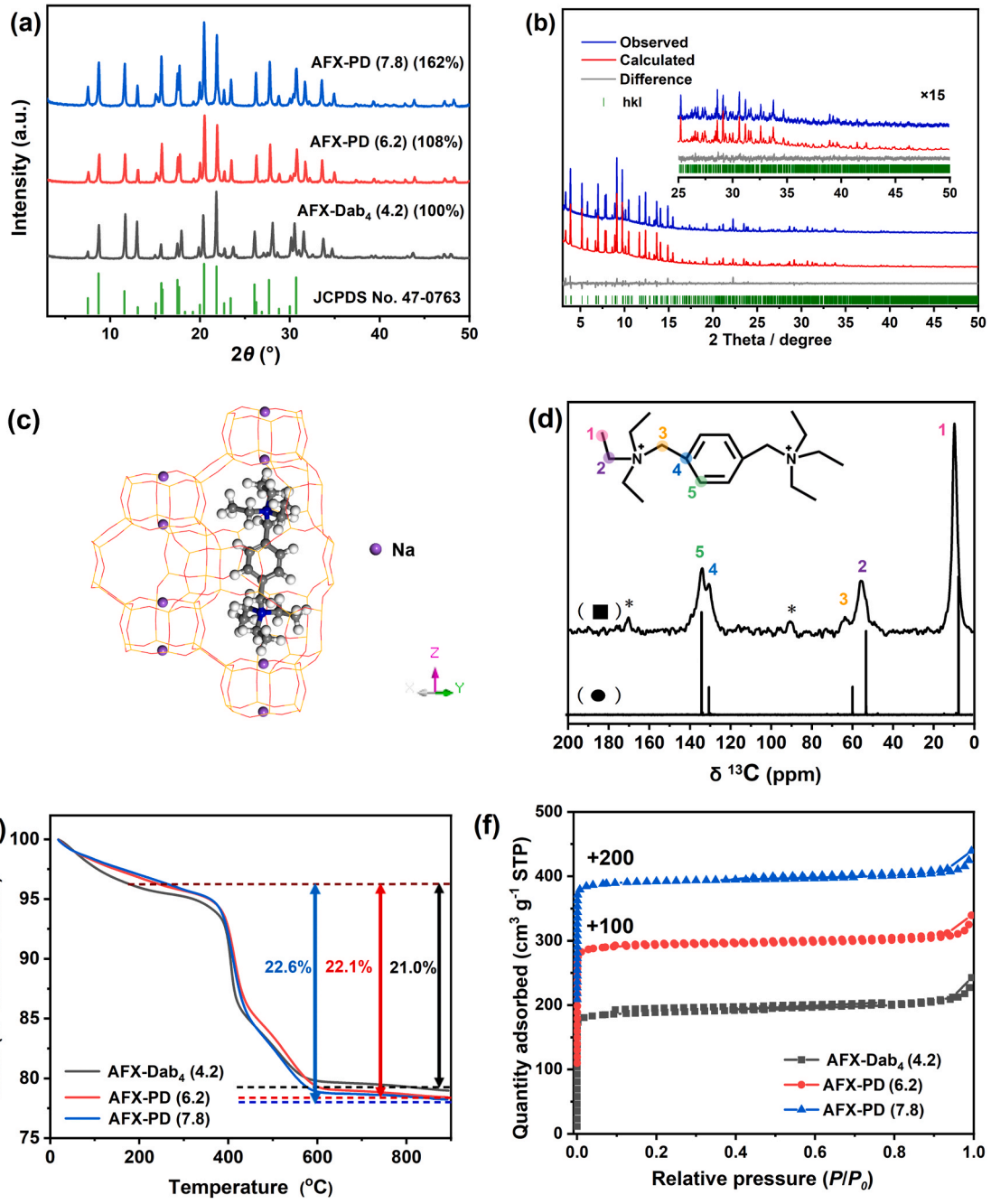


**Fig. 2.** XRD patterns for typical **AFX** zeolite derived from AFX-PD (6.2) and AFX-PD (7.8) and the control AFX-Dab$_4$ (a). OSDA as-made AFX-PD (7.8): observed (blue line), calculated (red line), and difference (grey line) powder synchrotron diffraction patterns. The tick marks indicate the positions of allowed reflections (b). $Na^+$ and PD cations are located apart inside the *gme* and the *aft* cages (c). $^{13}C$ MAS NMR spectra of PD occluded in AFX-PD (7.8) (black round) and $^{13}C$ NMR for PD dissolved in $D_2O$ (black square) (d). TGA curves of as-synthesized samples, and the weight losses shown in the inset correspond to exothermic combustive removal of OSDAs (e). $N_2$ physisorption isotherms for calcined samples (f). Symmetrical asterisk represents the spin sideband in (d).

**Table 1**
Lattice parameter, textural properties of **AFX** zeolites derived from $N_2$ physisorption and synthetic yield for as-synthesized **AFX** zeolites.

| Samples | Lattice parameters (Å) | | $S_{BET}$ ($m^2 \cdot g^{-1}$)[a] | $V_{micro}$ ($cm^3 \cdot g^{-1}$)[b] | $V_{total}$ ($cm^3 \cdot g^{-1}$)[c] | Yield (%) |
|---|---|---|---|---|---|---|
| | ***a*** | ***c*** | | | | |
| NaAFX-Dab$_4$ (4.2) | 13.77 | 19.96 | 528 | 0.26 | 0.35 | 43% |
| NaAFX-PD (6.2) | 13.65 | 19.92 | 536 | 0.27 | 0.34 | 55% |
| NaAFX-PD (7.8) | 13.52 | 19.89 | 562 | 0.27 | 0.36 | 62% |

[a] Calculated by the BET method
[b] Deduced by the *t*-plot method
[c] Calculated from NLDFT method.

performed against the diffraction patterns. To figure out different guest species occluded in the as-synthesized zeolite, the Rietveld refinement was carried out with a commercial TOPAS V5.0 suite. After optimizing the crystal framework, the residual electron density map was generated, and the missing guest species were filled in the empty zeolite cages (Fig. S1, SI). Sequentially, the Rietveld refinement was performed with the 37 soft geometric restraints imposed on the whole zeolite framework with proper penalty weight shown in Fig. 2b. As the refinement process progressed, the penalty weight was gradually removed. Finally, the crystallographic Data for AFX-PD (7.8) of whole matrix converged to a reasonable value: $R_{exp}$: 2.69%, $R_{wp}$: 4.88%, $R_p$: 3.42%, GOF: 1.81, as outlined in Table S2. In the as-synthesized **AFX** zeolite, there is no PD occluded in the *gme* cage, since the small cage can not accommodate the bulky PD, which could only occupy the *aft* cages. $Na^+$ and PD cations are located apart co-planar in the center of *d6r* ring and the *aft* cages, respectively (Fig. 2c). One may expect that the charge compensating $AlO_4^-$ sites also sit away from each other, therefore, lowering the possibility for the formation of hydrothermally vulnerable Al-O-Si-O-Al sites (i.e., vide infra, NMR detectable $Q^4$ = [$Si(OSi)_2(OAl)_2$ sites]. In fact, from the obtained structure model (Fig. S2 and Table S3), N-atom in ammonium groups of PD is found to locate inside *aft* cage with the nearest neighbor O atoms having a distance of ca. 4.00 Å. One may expect that the counterbalancing $AlO_4^-$ sites to sit between them, which is less likely to form Al pair sites with these sitting in the 6-MRs.

To confirm that it was PD, instead of the decomposed molecules that functioned as OSDA in the hydrothermal synthesis, the $^{13}C$ CP MAS NMR spectra of representative, as-synthesized AFX-PD (7.8) was recorded (Fig. 2d). The resonance peaks, with chemical shifts at 9, 52, 59, 129, 132 ppm, are assignable to the five types of carbon atoms in the structure, -($\mathbf{C}H_3$)$_3$, -$\mathbf{C}H_2$-$CH_3$, -$\mathbf{C}H_2$-$C_6H_4$, -**C**- and -**C**H- in the -$\mathbf{C}_6H_4$- ring, respectively. The relevant $^{13}C$ NMR spectra for PD dissolved in $D_2O$ is compared in the same Fig. 2d, which is essentially the same as the occluded one, thus, corroborating that PD is stable in the hydrothermal synthesis and is capable of directing the crystallization of **AFX** zeolite. The corresponding TGA curves are also determined, as displayed in Fig. 2e. The endothermic weight losses below 200 °C are often attributed to dehydration, and the broad, exothermic weight loss starting from 400 °C, ending at 600 °C can be ascribed to the combustive removal of OSDA , with weight loss of 21%, 22.1% and 22.6%, for NaAFX-Dab$_4$ (4.2), NaAFX-PD (6.2) and NaAFX-PD (7.8), respectively. Elemental compositions of as-synthesized samples derived from ICP-AES measurements are outlined in Table S4. These measurements allow the unit cell compositions to be determined as NaAFX-Dab$_4$ (4.2) (|$Na_{1.23}$-$Dab_{2.02}$-$(H_2O)_{15}$ |[$Si_{38.71}Al_{9.29}O_{96}$]-**AFX**), NaAFX-PD (6.2) (|$Na_{1.04}$-$PD_{2.71}$-$(H_2O)_{12}$|[$Si_{41.54}Al_{6.46}O_{96}$]-**AFX**) and NaAFX-PD (7.8) (|$Na_{0.74}$-$PD_{2.35}$-$(H_2O)_{11}$|[$Si_{42.57}Al_{5.43}O_{96}$]-**AFX**).

The textural properties for the calcined samples are probed by $N_2$ physisorption measurements and the isotherms are displayed in Fig. 2f. These isotherms can be classified to be type I isotherm with characteristic micropore filling occurring at $P/P_0 < 0.01$, due to the solely presence of micropores. The micropore volumes extracted from *t*-plot method, the BET surface area, total pore volume, as well as external surface area are tabulated in Table 1. The micropore volumes, indicative of crystallinity of zeolitic crystals, are identical for these samples (~0.26 $cm^3 \cdot g^{-1}$), recommending their high crystallinity. The BET surface area for AFX-PD (7.8) (562 $m^2 \cdot g^{-1}$), is measured to be larger than that of AFX-PD (6.2) (536 $m^2 \cdot g^{-1}$) and AFX-Dab$_4$ (4.2) (528 $m^2 \cdot g^{-1}$), as a result of decreased crystal size, as also advocated by the increase of external surface area. The synthesis yields are deduced from inorganic basis, which are, for the generation of NaAFX-Dab$_4$ (4.2), NaAFX-PD (6.2) and NaAFX-PD, respectively, to be 43%, 55% and 62%. The use of **FAU** zeolite as Al source brings about two benefits, an increase of framework Si/Al ratio and a high yield in synthesis. In the first place, **FAU** zeolite dislodges into *d6r* units, which is a building block for the product **AFX** zeolite. The release of these units therefore accelerates the formation of product, and the Si/Al ratio in these units may also be inherited into the daughter **AFX** zeolites. Here, it is observed that the yield has been significantly promoted by lowing the $Na^+$/Si ratio in the starting materials, because high alkalinity in supernatant solution solubilizes raw materials to a greater extent and lowers the solid yield accordingly. The fact that synthetic yields in our synthesis are higher than these reported using high alkali media advocates such explanations [28]. The synthetic yield is slightly higher (66%) when merely **FAU** zeolite is used as precursor in an inter-zeolite conversion route [29], since zeolite has low solubility in the mother liquor with respect to that of raw inorganic materials, i. e., they are mostly transformed into the product **AFX** zeolite.

Solid state MAS NMR is employed to determine the chemical environment of constituent atoms for both the as-synthesized and calcined samples. Fig. 3 A, C and E show only one prevalent resonance peak at 56 ppm, assignable to the tetrahedrally incorporated $AlO_4$ moieties, which can be distinguished for as-synthesized samples from the $^{27}Al$ MAS NMR spectra. Extra-framework, octahedrally coordinated species with weak chemical shift at 0 ppm can also be perceived from the calcined sample, owing to slight dealumination in the calcination process. $^{29}Si$ MAS NMR spectra (Fig. 3B, D, F) can be deconvoluted into three resonance peaks centered at − 110.8, − 104.4 and 98.5 ppm, corresponding to, respectively, $Q^4$ = [Si-$(OSi)_4$], $Q^4$ = [Si-$(OSi)_3(OAl)$] and $Q^4$ = [Si-$(OSi)_2(OAl)_2$], respectively. The respective concentrations are outlined in Table S5, showing that more single sites are generated as a consequence of increased framework Si/Al ratio. By using Eq. (1), it is possible to deduce the framework Si/Al ratios for these as-synthesized (and calcined) samples, which are 4.2 (for calcined sample, 4.0), 6.2 (6.0) and 7.8 (7.8), for AFX-Dab$_4$ (4.2), AFX-PD (6.2) and AFX-PD (7.8), respectively, and are essentially identical to that measured by chemical analysis. By comparing NMR generated Si/Al ratios for as-synthesized and calcined samples, it is seen that calcinations have insignificant impact on framework Si/Al ratios. Thus, the NMR data confirmed the successful generation of Si-rich **AFX** zeolites, which agree well with XRD and chemical analysis data.

Field-Emission Scanning Electronic Micrographs (FE-SEM), as displayed in Fig. 4b-c, reveal that NaAFX-PD (6.2) and NaAFX-PD (7.8) samples comprise of uniform bipyramid shaped particles of ca. 300–500 nm and 200–300 nm, i.e., crystal size decreases with increasing Si/Al ratio. In contrast, the control sample AFX-Dab$_4$ (4.2) displayed in Fig. 4a consists of smaller (250–300 nm), irregularly shaped particles. Typical low magnification TEM images for NaAFX-PD (7.8) are exhibited in Fig. 4d, bipyramidal intergrown crystal of can be clearly visualized. The High Resolution TEM micrographs images are taken perpendicular to [110] and [210] axes, respectively, as corroborated by the SAED patterns (Fig. 4e-f), ordered cages (white spots) and lattice frameworks (dark areas) can be distinguished. The corresponding structure models are overlapped with these images and agree excellently well with the observed patterns, verifying the highly ordered, crystalline framework structures.

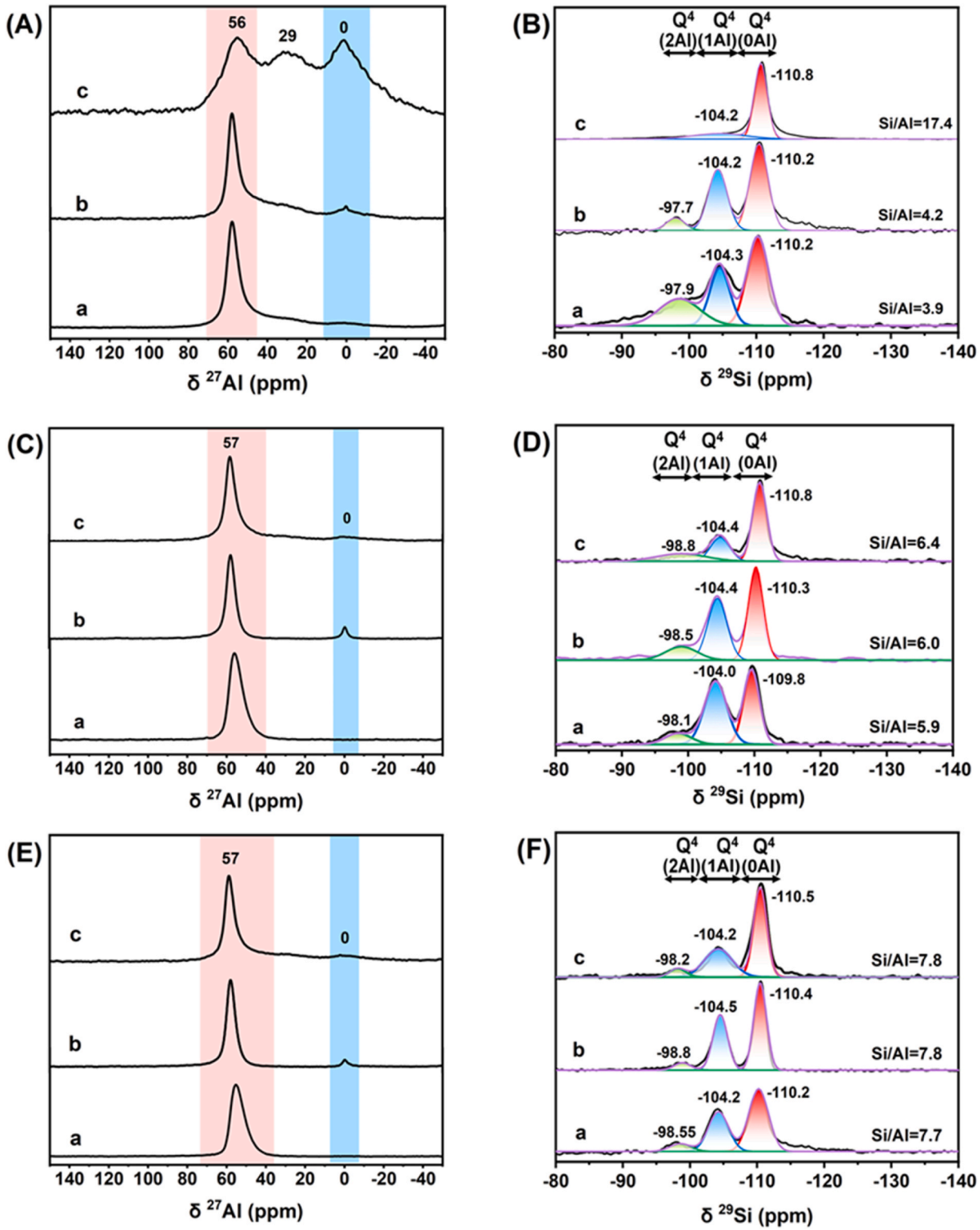


**Fig. 3.** Solid state $^{27}$Al MAS NMR spectra (A, C, E) and $^{29}$Si NMR spectra (B, D, F) for as-synthesized (a) calcined (b) and hydrothermally treated (850 °C for 10 h) (c) AFX-Dab$_4$ (4.2), AFX-PD (6.2) and AFX-PD (7.8).

After ion-exchanging the samples to their proton types, ammonia temperature programmed desorption ($NH_3$-TPD) patterns were acquired to probe the influence of framework compositions on the acidity of samples, as illustrated in Fig. S3. Each of the proton type zeolite (Fig. S3 a and b) TPD profile can be divided into two broad desorption peaks in the low (150–300 °C) and high (400–700 °C) temperature regions, corresponding to, respectively, desorption from weak acid sites of surface silanol and defects and these of strong acid sites. High temperature desorption maxima are detected at 526 °C, 530 °C and 530 °C, for HAFX-Dab$_4$ (4.2), HAFX-PD (6.2) and HAFX-PD (7.8), respectively, recommending that increase of framework Si/Al ratio and crystallinity has enhanced the acid strength of the latter samples. As $NH_3$-TPD can only provide information of acid strength, $NH_3$-IR spectroscopy as a complementary technique is employed to discriminate and quantify

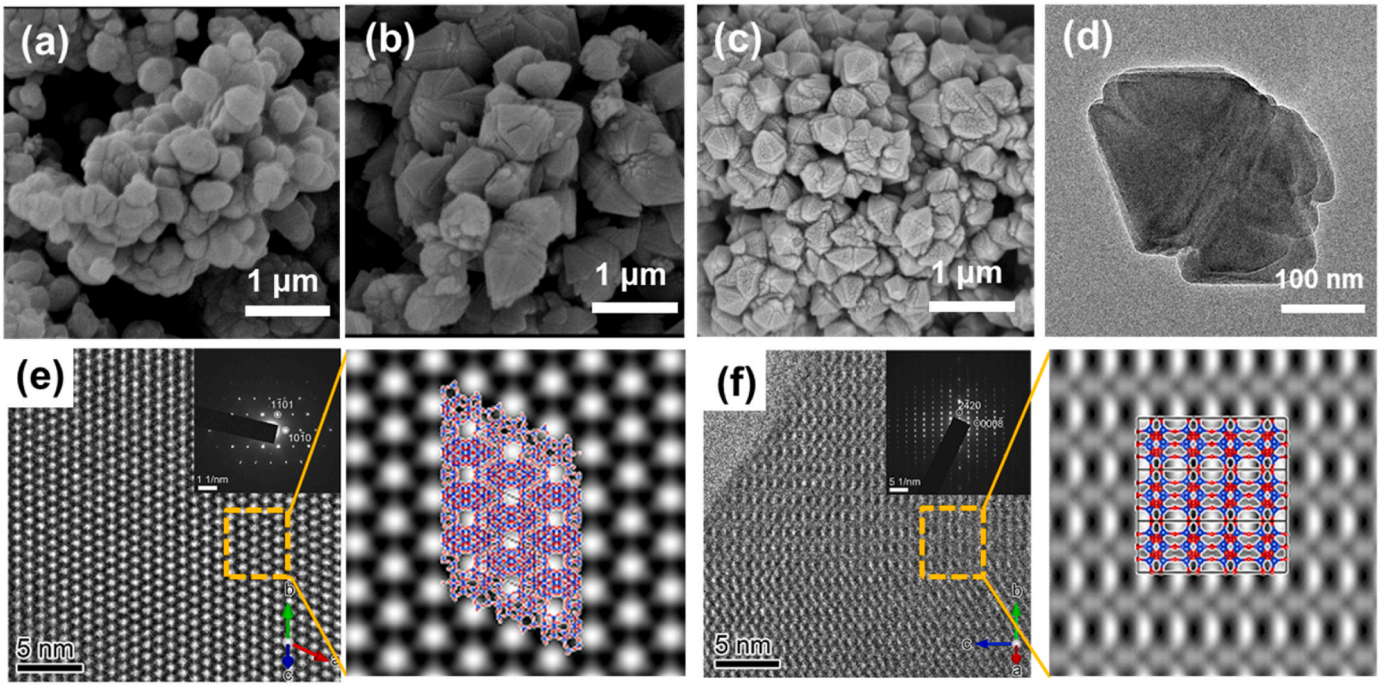


**Fig. 4.** FE-SEM micrographs of AFX-Dab$_4$ (4.2) (a) AFX-PD (6.2) (b) and AFX-PD (7.8) (c). HR-TEM of representative AFX-PD (7.8) (d) and the corresponding SAED patterns taken from ***c***- and ***a***- axes, with the structural models shown in (e) and (f) respectively.

Brønsted (BAS) and Lewis (LAS) acid sites, as depicted in Fig. 5a-b. $NH_3$ was chosen as a probe molecule for its small size that allowed entering into the cages through the small pore apertures, since often used pyridine was too large to have access. The spectra collected after desorption at relatively low temperature of 150 °C were used to estimate the total amount of acid sites ranging from weak to strong ones, while the number of medium-to-strong acid sites were deduced from the data collected after desorption at 300 °C. The extracted numbers of acid site density for these samples are listed in Table S6. Numbers for the medium-to-strong BAS that are catalytically important follow the decremental order of HAFX-Dab$_4$ (4.2) (3565 μmol·g$^{-1}$) > HAFX-PD (6.2) (3148 μmol·g$^{-1}$) > HAFX- PD (7.8) (2488 μmol·g$^{-1}$), albeit the less total numbers of BAS have been measured for HAFX-Dab$_4$ (4.2). Overall, the Si-rich HAFX-PD (7.8) sample is disclosed to possess less, but more medium-to-strong BAS with respect to the control sample.

The proton type samples were also ion-exchanged into their $Cu^{2+}$-exchanged forms to afford fresh catalysts, for which characterizations were made to determine the nature of copper species. The contents of Cu determined using ICP-AES method to be 3.2 wt%, 3.1 wt% and 3.4 wt%, equivalent to Cu/Al ratios of 0.47, 0.63 and 0.89 (Table S4), for CuAFX-Dab$_4$ (4.2), CuAFX-PD (6.2) and CuAFX-PD (7.8), respectively. Fig. 6a shows the Cu($2p_{3/2}$) XPS spectra of fresh CuAFX-Dab$_4$ (4.2), CuAFX-PD (6.2) and CuAFX- PD (7.8). Two peaks centered at 933.7 eV, and 936.2 eV, assignable to the $Cu^+$ in $Cu(OH)^+$ and $Cu(OH)_2$ (possibly Cu$(OH)^+$-Z) like environments, respectively, are observable in the spectra of the three fresh catalysts. Besides, a shake-up satellite peak is identified with binding energy around 945 eV, typical of $Cu^{2+}$ due to the ligand to metal (O(2p)→Cu(3d)) electron transfer [61]. The formation of $Cu_2O/Cu^0$ species on the surface of each catalyst is attributable to the reduction of $Cu^{2+}$ ions by X-ray irradiation [62]. The peak at 933.7 eV has been assigned to the $Cu^+$ ions coordinated to the zeolite framework oxygen atoms. The relative distributions of Cu species present on the surface of zeolite catalysts employed here have been determined by deconvolution of the XPS spectra. Clearly, all three fresh and hydrothermal treated catalysts possess both $Cu^{2+}$ and $Cu^+$ ions.

In the corresponding $H_2$-TPR patterns, as exhibited in Fig. 6b and 6c, one peak centered at ~230 °C, likely due to the reduction of $Cu^{2+}$-Z2 or $Cu(OH)^+$-Z tethered on $AlO_4^-$ sites close to the 6-MR to afford $Cu^+$-Z, can be distinguished on all fresh samples [62]. It is likely that more Cu$(OH)^+$-Z species exist in samples with higher Si/Al ratios, since they have less paired Al sites to be exchanged to $Cu^{2+}$-Z2. The reduction peak is found to be invariant to changes of framework Si/Al ratio, and there is no $CuO_x$ or $CuAl_2O_4$ phases in these samples. The structure model for which is schematically illustrated alongside the reduction peak. Besides, high temperature reduction peaks appearing at 900 to 950 °C are also distinguishable, which is often attributed to reduction of $Cu^+$-Z to the metallic $Cu^0$ state (> 900 °C). Collectively, highly reducible, $Cu(OH)^+$-Z or $Cu^{2+}$-Z2 tethered on $AlO_4^-$ sites has been determined to be the major surface component over all fresh catalysts.

### 3.3. The hydrothermal stability test

To access the influence of Si/Al ratio on hydrothermal stability, accelerated hydrothermal aging were conducted for Cu-exchanged **AFX** zeolites, at 750 °C for 24 h and 850 °C for 10 h, respectively, as detailed in the experimental section. Such high temperatures are regarded sufficient to testify the hydrothermal stability for use as $NH_3$-SCR catalyst under harsh conditions. Hydrothermal aging at either 750 °C or 850 °C has caused the structural collapse for control CuAFX-Dab$_4$ (4.2) sample, due to the low Si/Al ratio and poor hydrothermal stability, as shown by the XRD data (Fig. S4). In contrast, both the high-silicon CuAFX-PD (6.2) and CuAFX-PD (7.8) were found to be robust after the same treatments. By defining the RC for CuAFX-PD (6.2)-fresh to be 100%, the variation for RCs after these treatments can be compared. The RC values were measured to be 83% and 107%, for CuAFX-PD (6.2)-HT750 and CuAFX-PD (7.8)-HT750, respectively, while inferior RC were determined for CuAFX-PD (6.2)-HT850 (71%) and CuAFX-PD (7.8)-HT850) (78%). Furthermore, the impacts of hydrothermal treatment on framework structure were measured by $^{27}$Al and $^{29}$Si MAS NMR (Fig. 3). Only insignificant dealumination was detected over hydrothermally treated AFX-PD (6.2) and CuAFX-PD (7.8) samples (Fig. 3 C, E), which was strikingly different from the collapsed AFX-Dab$_4$ (4.2), from which a large proportion of extra-framework Al species could be observed (Fig. 3A). After deconvolution of $^{29}$Si MAS NMR data for AFX-PD (6.2)

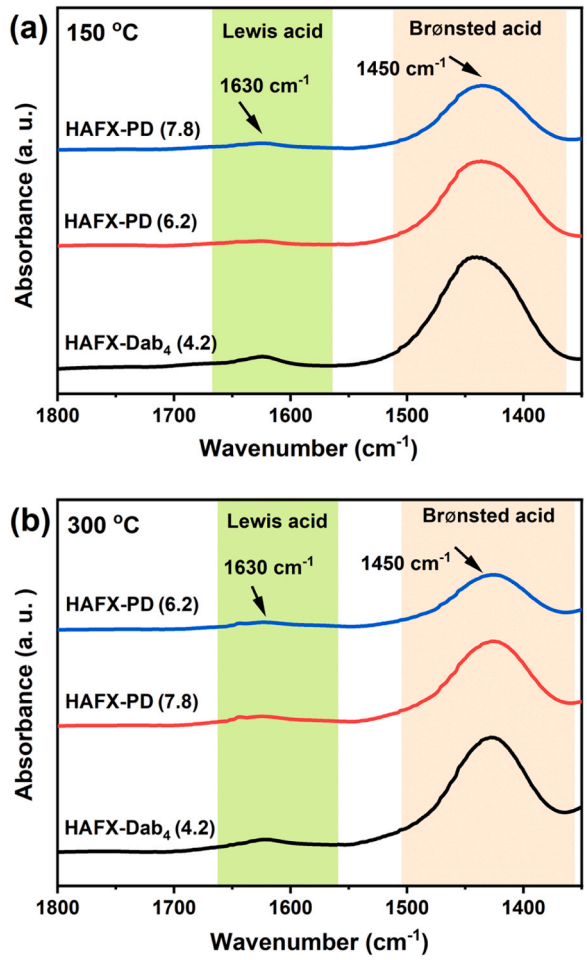


**Fig. 5.** $NH_3$-IR spectra collected after desorption at 150 °C (a) and 300 °C (b) on HAFX-$Dab_4$ (4.2), HAFX-PD (6.2) and HAFX-PD (7.8). The quantification of acidity is outlined in Table S6.

and CuAFX-PD (7.8) samples (Fig. D, F), the framework Si/Al ratios could be deduced, which were found to be essentially intact with respect to the fresh counterparts. Such deconvolution also allowed the concentrations of $Q^4 = [Si(OSi)_2(OAl)_2]$ sites to be determined, which were compiled in Table S5. Hydrothermal treating at 850 °C has slightly increased the amount of $Q^4 = [Si(OSi)_2(OAl)_2]$ sites in AFX-PD (6.2) from 14% (for calcined sample) to 19%, while concentrations for these sites remains low on AFX-PD (7.8) (7%), hence, proving the high stability for the latter. The comparisons demonstrate that increase of framework Si/Al ratio has marked enhanced the hydrothermal stability of these high-silicon samples.

To correlate the hydrothermal stability with structural features, we have compared the RC values, $Q^4 = [Si(OSi)_2(OAl)_2]$ sites concentrations for fresh and hydrothermal treated samples, as shown in histogram in Fig. 7c. The RC values for fresh samples are found to increase with increasing Si/Al ratios of their frameworks. Meanwhile, the concentration for the hydrothermally vulnerable paired Al sites tend to decrease. For the hydrothermally aged samples, the same trend has also been observed. Therefore, the silicon-rich **AFX** zeolite framework is more stable mainly for two reasons: a high inherent crystallinity and a lowered concentration for the paired Al sites.

The hydrothermally treated (850 °C for 10 h) Cu-type catalysts were also subjected to $H_2$-TPR measurements, to reveal possible site structure change upon hydrothermal heating, as displayed in Fig. 6c. The low temperature reduction profiles can be roughly divided into two overlapping ones, centered at ~250 and 350 °C, which can be attributed to reduction of $Cu^{2+}$-Z2 or $Cu(OH)^+$-Z situated close to 6-MR (vide infra, $NH_3$-IR). Here the shift towards higher temperature can be tentatively attributed to the migration of $Cu(OH)^+$ from the *aft* cage to *gme* cage. This assignment is plausible because smaller cage confinement often exerts better stabilization, and hence, resistance towards reduction. In fact, $Cu(OH)^+$ ions sitting at 6-MR form the predominant species in the CuAFX-PD (7.8) sample and the reduction of insignificant amount of $Cu^{2+}$ locating close to 8-MR can not produce the prominent reduction peak. Neither could it be the reduction of $CuO_x$ clusters or $CuAl_2O_4$, whose reduction often requires higher temperatures. The concentrations for $CuO_x$ clusters or $CuAl_2O_4$ should be negligible as $Cu(OH)^+$ sitting close to 6-MR is the major component in the fresh catalysts, which is stable to hydrothermal treatment, and also because formation of large amount of these species often suggests framework collapse [62]. The reduction of $Cu^+$-Z to $Cu^0$ is essentially identical to that of the fresh catalysts, indicating that reducibility for $Cu^+$-Z species is less affected by steaming. In course of hydrothermal aging, part of the $Cu^{2+}$-Z2 or $Cu(OH)^+$-Z species in the *aft* cages may have migrated to the 6-MR sites, driven by a stronger stabilization[63]. In situ FTIR of $NH_3$ adsorption are used to investigate the nature of Cu species, as displayed in Fig. 6d, the two negative peaks at ~900 and 950 $cm^{-1}$ are assignable to T-O-T vibrations perturbed by the presence of isolated $Cu^{2+}$-Z2 (or $Cu(OH)^+$-Z) moieties siting close to 6-MR and T-O-T vibrations perturbed by $Cu^{2+}$-Z2 (or $Cu(OH)^+$-Z) next to 8-MR, respectively [64,65]. In the fresh catalysts, intense absorption of 897 and 900 $cm^{-1}$ bands, together with a weak 948 $cm^{-1}$ band, can be distinguished, indicating that $Cu^{2+}$ largely locates at sites close to 6-MR, together with marginal ones populated at the 8-MR. After hydrothermal aging, the intensity of the former has weakened, while the copper species at the 8-MR vanish, manifesting that $Cu^{2+}$-Z2 (or $Cu(OH)^+$-Z) species situated close to 6-MR constitute the major sites after hydrothermal aging, despite of its the reduced concentration. Complementarily, CO absorption IR has also been used to probe the identity of copper, as displayed in Fig. S6, only one absorption band at 2157 $cm^{-1}$ resulting from di-carbonyl complexed $Cu^+$-Z locating in constrained environments can be visualized, as revealed in Fig. S6 [66]. Collectively, $Cu^+$-Z and $Cu^{2+}$-Z2 (or $Cu(OH)^+$-Z) are found to predominate in the vicinity of 6-MR, together with marginal population close to 8-MR in the fresh catalysts, while they only occupy the 6-MR sites after hydrothermal treating. This preferential occupation is likely due to that (1) the 6-MR sites interact strongly with copper moieties, and (2) hydrothermal treating causes framework dealumination to $AlO_x$ species and their preferential combination to weakly bound $Cu^{2+}$ species close to the 8-MR to form, negligible amount of extra-framework $CuO_x$ or $CuAl_2O_4$, for the low concentrations of $Q^4 = [Si(OSi)_2(OAl)_2]$.

This explanation is also advocated by $NH_3$-TPD measurements for fresh and hydrothermally treated samples, as compared in Fig. S3c and d. Each of the Cu-type zeolite TPD profile can be divided into three broad desorption peaks: the peak in the low temperature region ( < 300 °C) is attributed to $NH_3$ at the weak acid site. The peak in the mid-temperature region of ca. 400 °C is attributed to $NH_3$ on Cu species. The peak in the high temperature region at about 500 °C is attributed to the desorption peak of $NH_3$ at the strong acid site [67,68]. $NH_3$ desorption from residue, un-exchanged BAS can be clearly distinguished at ca. 530 °C as shoulder peaks, which virtually disappear into the base line after hydrothermal treatment at 850 °C, as a result of $Cu^{2+}$ migration and ion-exchange with BAS [69]. As $Cu^{2+}$ sitting in the 6-MR has been found to enhance the hydrothermal stability of zeolite framework, the redistribution of $Cu^{2+}$ and formation of such sites are likely a further boost of structure hydrothermal stability.

### 3.4. Catalytic performance in $NH_3$-SCR

#### 3.4.1. The proton-form AFX zeolite

Recently, it has been demonstrated that metal free, H-AFX zeolite alone also form a catalyst for $NH_3$-SCR [70], we therefore decided to exam the catalytic performance of H-AFX catalysts first. As our synthetic

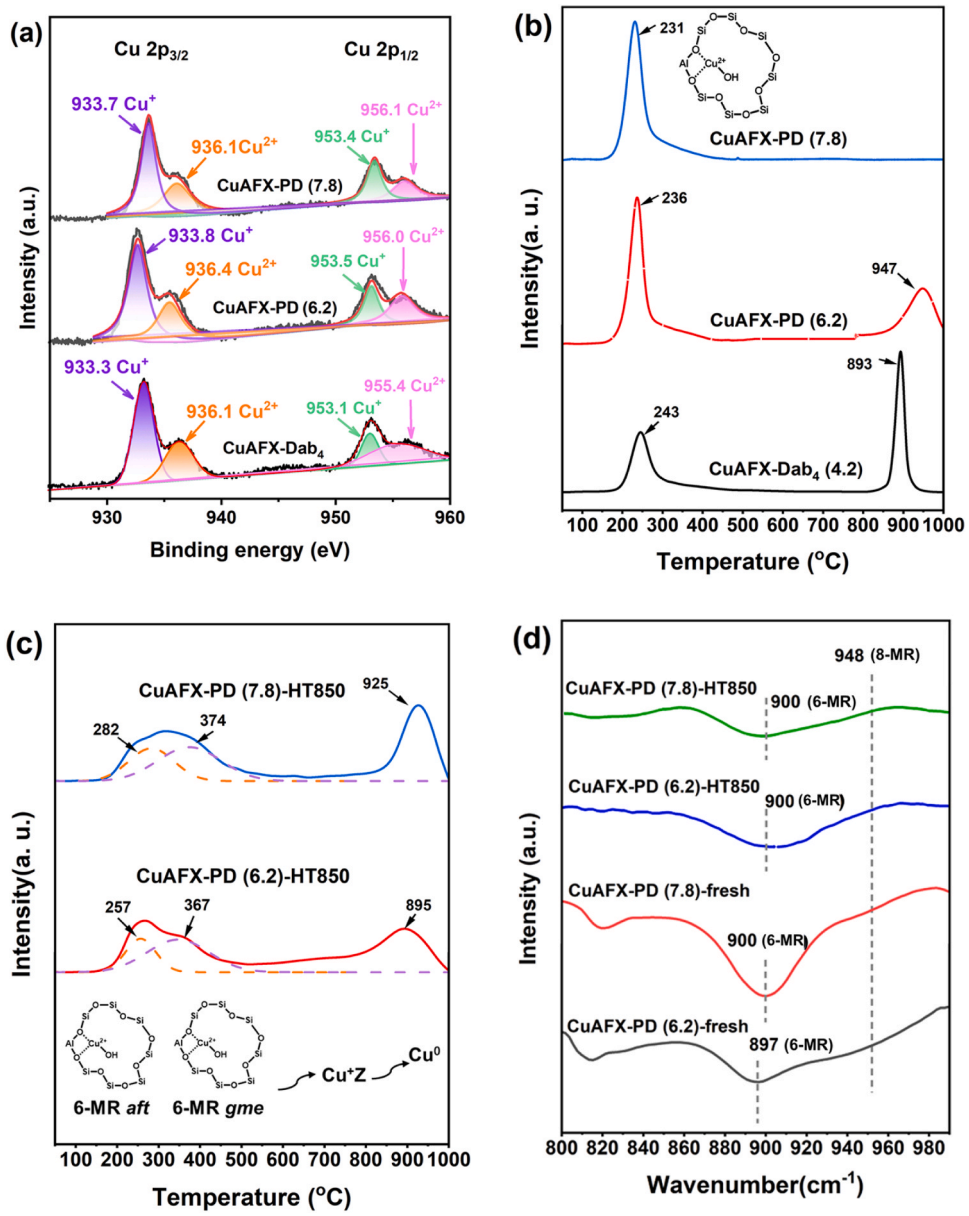


**Fig. 6.** Determination of chemical states for Cu in Cu-AFX zeolites using XPS spectra (a), $H_2$-TPR for the fresh CuAFX-Dab$_4$ (4.2), CuAFX-PD (6.2) and CuAFX-PD (7.8) samples (b) and the hydrothermal treatment (850 °C for 10 h) CuAFX-PD (6.2)-HT850 and CuAFX-PD (7.8)-HT850 samples (c), in situ FTIR of $NH_3$ adsorption at 100 °C for fresh CuAFX-PD (6.2) and CuAFX-PD (7.8) samples and the hydrothermal treatment (850 °C for 10 h) CuAFX-PD (6.2)-HT850 and CuAFX-PD (7.8)-HT850 samples (d).

method allowed the Si/Al ratio to be manipulated, the influence of acid sites density could be inspected as well. The catalytic performances were evaluated on both the fresh and hydrothermally treated H-AFX catalysts (850 °C for 10 h), under typical standard SCR conditions: 500 ppm $NH_3$, 500 ppm NO, 15% $O_2$, 10% $H_2O$ balanced with $N_2$ with a GHSV of 200, 000 g-NO·(g-cat·h)$^{-1}$, from 100 to 600 °C, as manifested in Fig. 8. The main product is found to be $N_2$, with a selectivity above 90%, together with formation of $N_2O$ as byproduct. On fresh H-AFX zeolites, $NO_x$ conversions are found to increase with temperature below 350 °C over all catalysts, and an activity order of HAFX-PD (6.2) (from 5%−31%) > HAFX-PD (7.8) (from 4%−23%) > HAFX-Dab$_4$ (4.2) (from 7%−18%) can be observed, with the latter being less reactive for the low acid strength.. Concomitantly, a reverse order for $N_2O$ selectivity has been detected. In the temperature regime above 350 °C, the activity levels off and a concurrent increase for $N_2O$ selectivity, can be perceived, owing to partial degradation of intermediate $NH_4NO_3$ in the absence of NO. On the two hydrothermally treated catalysts, HAFX-PD (6.2)-HT850 and HAFX-PD (7.8)-HT850, as shown in Fig. 8d, lowered activities, but increased $N_2O$ selectivity have been measured, since hydrothermal treating causes dealumination of framework (referring to $^{27}$Al MAS NMR) and a consequent decrease in acid site density. It is therefore concluded that catalytic activity for BAS catalyzed NO conversion is highly dependent on acid site density, and unwanted $N_2O$ formation can be mitigated over catalysts with high acid site density.

The structure-catalysis relationship has been considered on basis of reaction mechanism [70], as explained in Fig. 8e. NO is oxidized by the co-fed $O_2$ to afford more reactive $NO_2$ (a likely kinetically important step), which further react with $NH_3$ catalyzed by BAS to form $N_2$, $H_2O$, and intermediate $NH_4NO_3$. $NH_4NO_3$ can either react with NO to generate $NO_2$ and another intermediate $NH_4NO_2$, or, alternatively, undergoes decomposition to produce $N_2O$ in the absence of NO. The generated $NH_4NO_2$ may decompose readily into $N_2$ and $H_2O$. With

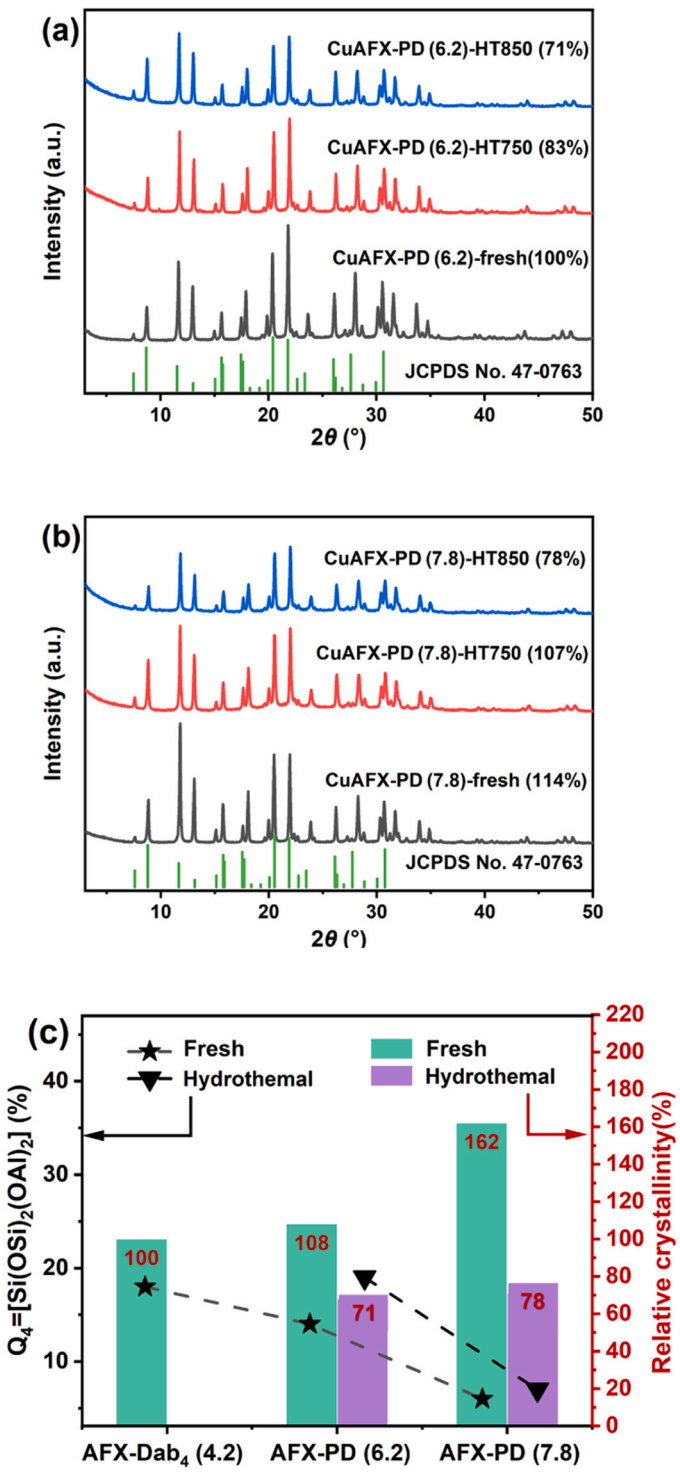


**Fig. 7.** XRD patterns of the CuAFX-PD (6.2)-fresh, after hydrothermal treatment at 750 °C for 24 h and 850 °C for 10 h (a). CuAFX-PD (7.8)-fresh, after hydrothermal treatment at 750 °C for 24 h and 850 °C for 10 h (b). The corresponding RC values are shown in the insets. The tendency of relative crystallinity and Si sites inferred from $^{29}$Si MAS NMR deconvolution (c).

lowered BAS density, $NH_4NO_3$ may accumulate and the unwanted decomposition contribute to formation of more $N_2O$. As $NH_4NO_3$ surface concentration is temperature dependent, further increase of reaction temperature above 400 °C tend to lower the contribution from this reaction pathway.

### 3.4.2. Catalytic performance of Cu-AFX catalysts

**AFX** materials were exchanged with an aqueous solution of copper acetate to achieve a $Cu^{2+}$ loading of ~3.0 wt% (Table S4), which is usually considered an optimum for $NH_3$-SCR reaction [71]. Catalytic assessments were conducted under identical conditions as for proton type catalysts. Fig. 9a displays the $NO_x$ conversions and $N_2O$ selectivity variations as a function of temperature on the fresh CuAFX-Dab$_4$ (4.2) catalyst, and only $N_2$ and $N_2O$ have been detected as nitrogen containing products. At 100 °C, a conversion of 5% and a $N_2O$ selectivity of 1% is observed, which can be regarded as a contribution out of residue BAS catalyzed reaction, since Cu-type catalyst is often inactive at such low temperatures [72]. The activity is found to increase with increasing temperature rapidly from 150 to 300 °C, reaching > 80% conversion between 250 °C and 450 °C, with $N_2O$ selectivity lower than 3%, which can be regarded as the high activity temperature window. Above 500 °C, $NH_3$ oxidation by $O_2$ produces $N_2O$ as a byproduct, whose selectivity increases with increasing temperature [73]. As CuAFX-Dab$_4$ (4.2) collapsed after hydrothermal aging, we only report the catalytic activity of the fresh catalyst, which may stem from a combined contribution from both Cu-driven redox cycle and BAS-driven cycle.

The catalytic activities for fresh and aged CuAFX-PD (6.2) catalysts are compared in Fig. 9b. The fresh catalyst exhibits an onset temperature at 200 °C with a $NO_x$ conversion of 57%, and the conversion increases to 91% at 250 °C, leveling off with a close to 100% $NO_x$ conversion in the high activity temperature window from 300 °C (99%) to 480 °C (98%), before dropping at 500 °C, with a lowered $NO_x$ conversion (96%). The $N_2$ selectivity is noticed to exceed 95% in the high activity window. The 750 °C aged CuAFX-PD (6.2) catalyst shows a low initial activity at 100 °C ($NO_x$ conversion 6%) that increase to 19% $NO_x$ conversion from 150 °C on, and the high activity window is found between 200°C (58% $NO_x$ conversion) and 500 °C ($NO_x$ conversion of 84%). For the same catalyst, nevertheless, a higher $N_2O$ selectivity (varying from 5% to 7%) has been observed, likely due to the accumulation of $NH_4NO_3$. Over the 850 °C aged CuAFX-PD (6.2) catalyst, similar trend has been observed, but with a narrower activity window spanning from 300 °C ($NO_x$ conversion 92%) to 400 °C ($NO_x$ conversion 95%) and a decreased $N_2O$ selectivity (< 1%). After hydrothermal treating, the decay in low temperature activity leads to the narrowing of the window, which is often indicative of structural degradation and partial loss of active sites [74].

Fig. 9c reveals the catalytic activities for CuAFX-PD (7.8) series. At the onset temperature of 150 °C, the measured $NO_x$ conversions are, respectively, 69%, 65% and 57% over fresh, 750 °C and 850 °C aged catalysts, which can be increase to 97%, 94% and 86% at 200 °C. The fresh and 750 °C aged catalysts manifest comparable high activity window ranging from 200 °C to 515 °C, with only marginal selectivity to $N_2O$ (< 2%). Even the CuAFX-PD (7.8)-HT850 catalyst has a high activity window from 250 °C to 410 °C, with a $N_2O$ selectivity of 5%, which has been markedly expanded with respect to CuAFX-PD (6.2) catalyst, proving therefore a highly efficient catalyst. The contribution from residue BAS should be minimal for the remarkable reduced site density. For these aged catalysts with such high Si/Al ratio, the catalytic activity can be largely attributed to the contribution from Cu-driven redox cycle, since the BAS sites have been removed (evidenced by $NH_3$-TPD, Fig. S3d) because of ion-exchange. Fig. S5 and Table S7 show the textural properties of CuAFX-fresh and hydrothermally aged zeolites derived from $N_2$ physisorption. The BET surface area for CuAFX-PD (7.8)-fresh (602 $m^2 \cdot g^{-1}$), is measured to be larger than that of CuAFX-PD (6.2)-fresh (571 $m^2 \cdot g^{-1}$), as a result of increased relative crystallinities (100% to 114%, shown in Fig. 7a, b), as also advocated by the increase of pore volumes of the samples (0.39 $cm^3 \cdot g^{-1}$ and 0.42 $cm^3 \cdot g^{-1}$, respectively). Only subtle changes of surface area and pore volume are determined for the 750 °C and 850 °C hydrothermally aged samples, with respect to the fresh ones (Table S7), confirming their structural integrity. The preserved activity after hydrothermal aging can therefore be a consequence of structural integrity due to framework Si/Al ratio increase.

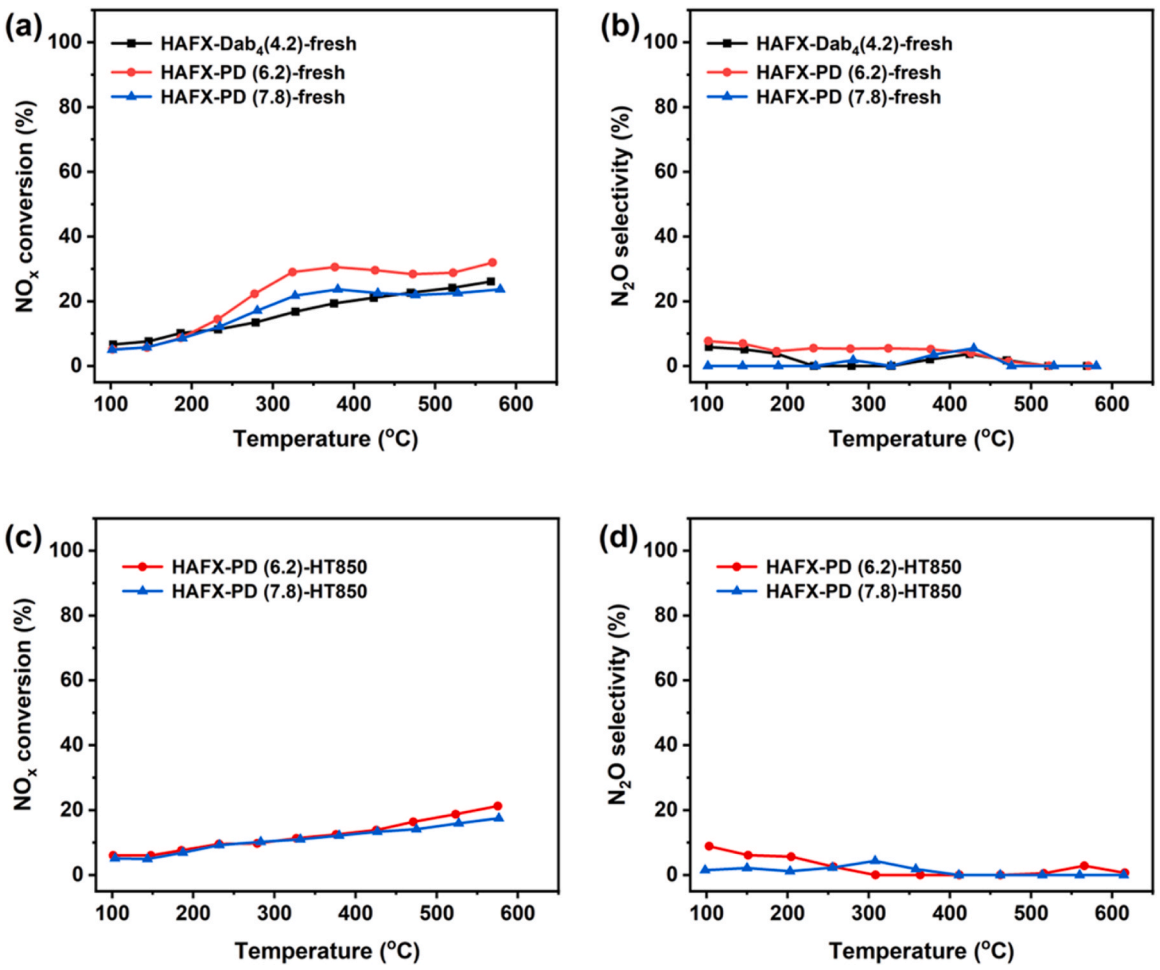


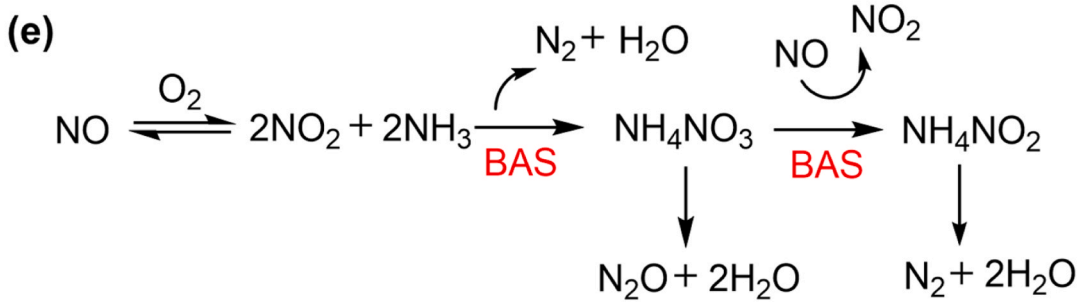


**Fig. 8.** Catalytic performance of proton-form, fresh (a) and hydrothermal treated 850 °C for 10 h (c) H-AFX zeolites in $NH_3$-SCR reaction, plotted as $NO_x$ conversion versus reaction temperature under typical conditions: 500 ppm $NH_3$, 500 ppm NO, 15% $O_2$, 10% $H_2O$ balanced with $N_2$ with a GHSV of 200,000 g-NO g-cat$^{-1}$·h$^{-1}$. The selectivity to $N_2O$ from unwanted side reaction is also displayed (b, d). Proposed mechanism for the $NH_3$-SCR reaction over proton-form (e).

Before discussing the structure-catalysis relationship for Cu-type catalyst, it is useful to consider the reaction mechanism. For the Cu-type zeolite catalyzed standard $NH_3$-SCR process, the catalytic activities are divided to low (150–300 °C) and high (> 300 °C) temperature regimes based on their varied mechanistic origins [75]. One plausible explanation for the high catalytic activity in the low temperature regime is that the *aft* cage has more than two $AlO_4^-$ sites on which $Cu(OH)^+$ can be electrostatically tethered and is sufficiently large to accommodate the formation of bulky copper dimers, thus avoiding the energetically demanding inter-cage diffusion (the barrier is of comparable magnitude to that of intrinsic catalytic process [76–78]. Here, formation of more than two $AlO_4^-$ sites can be expected from the occlusion of dicationic OSDA inside the *aft* cage, which entails to be charge-compensated. Meanwhile, cohabitation of two isolated $[Cu(NH_3)_2]^+$ cations within one cage may also facilitate their oxidative coupling (the rate determining step for low temperature regime reaction) to the formation of key intermediate $Cu(NH_3)_2$-$O_2$-$Cu(NH_3)_2$, as theoretical investigations anticipate that the individual copper cation cannot effectively combine with 9 Å distance away, neighboring ones, since cross cage migration is also a kinetically demanding process [75]. As CuAFX-PD (7.8)-HT850

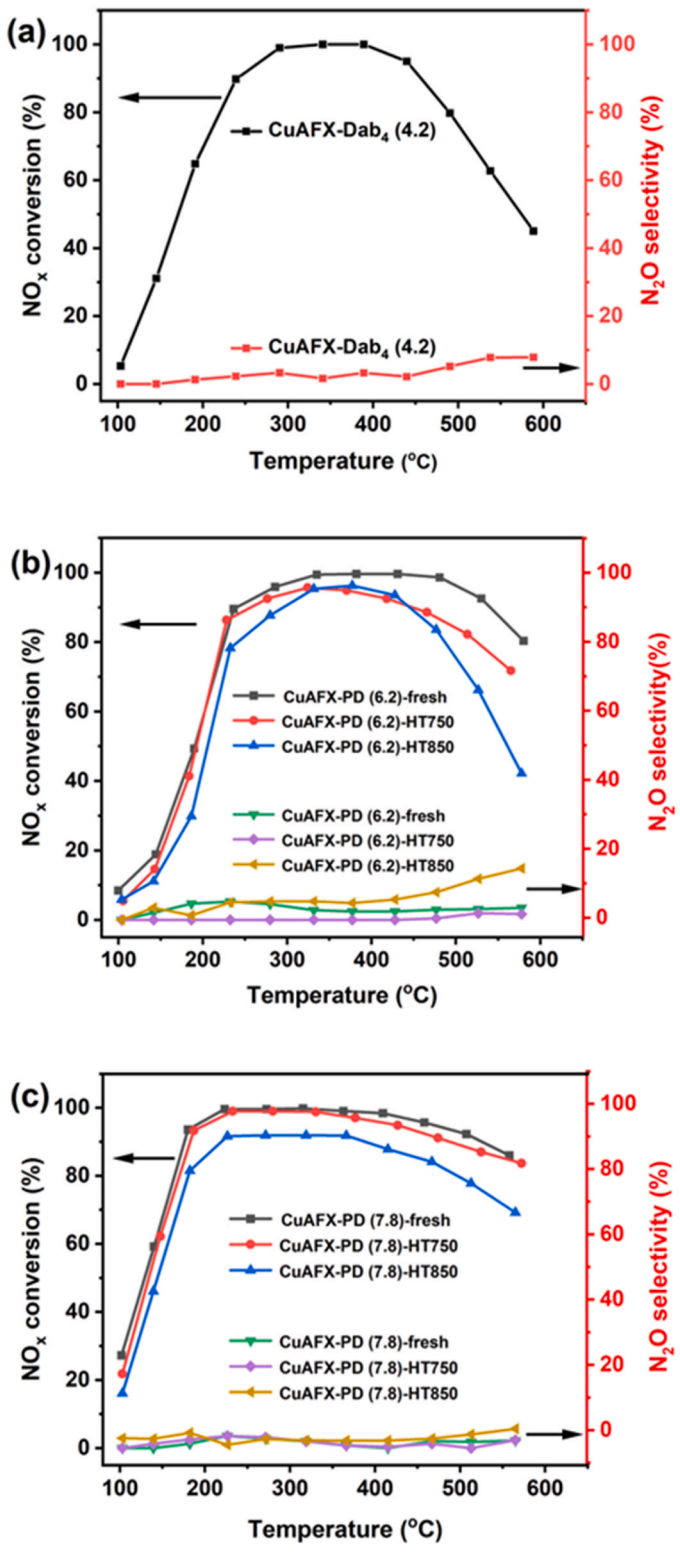


**Fig. 9.** Measured $NO_x$ conversion over CuAFX-$Dab_4$ (4.2)-fresh (a), CuAFX-PD (6.2)-fresh and hydrothermal treated (b), and CuAFX-PD (7.8)-fresh samples and hydrothermal treated (c). The selectivity to $N_2O$ from unwanted side reaction is also displayed.

comprises insignificant amount of proton sites (Fig. S3d), the observed activity stems predominantly from Cu-driven, redox catalytic cycle. Hence, the observed low temperature activity for fresh Cu-AFX catalyst may be attributed to the facile formation of kinetically important copper dimers endowed by the proximity of active sites inside the same *aft* cage.

The hydrothermal stability of Cu-exchanged zeolites can be influenced by two factors, i. e., the hydrothermal stability of zeolitic framework itself and the impact of Cu over it, of which the former plays a pivotal role. The influence of Si/Al ratio of framework stems from the facts that increased Si/Al ratio brings about presence of less steaming susceptible paired Al sites ($Q^4$ = $[Si(OSi)_2(OAl)_2]$), which dealuminate easily upon exposing to high temperature hydrothermal aging treatments [79]. In addition, as $Cu(OH)^+$ species sitting close to the 6-MR also exert a further stabilization effect, and the copper exchanged zeolites often have better hydrothermal stability with respect to their proton forms [80]. For the hydrothermal treated samples, $CuAlO_x$ formation between copper ions and extra-framework $AlO_x$ derived from dealumination out of paired Al sites has been regarded as the main cause of catalyst deactivation [81]. Fig. S7 illustrates the mechanism for the hydrothermal aging: paired Al sites (-Al-O-Si-O-Al-), i.e., $Q^4$ = $[Si\text{-}(OSi)_2(OAl)_2]$, can be dislodged from zeolite framework upon attacking by steam to produce extra-framework $AlO_x$ moieties. $AlO_x$ moieties may reaction with $Cu^{2+}$ species to generate $CuAlO_x$. This dealumination process generate defective sites whose concentration increase may cause framework collapse. Hence, the concentration of which represents an index for hydrothermal stability. The increase of Si/Al ratio has lowered the fraction of such pair sites and hence the propensity of catalyst deactivation due to loss of active sites. Here, the increase in Si/Al ratio has led to better crystallinity, lowered concentrations for such paired sites, which contribute together to the framework robustness. Moreover, the predominant distribution of $Cu^{2+}$-$^-$Z2 (or $Cu(OH)^+$-$^-$Z) at mainly the 6-MR, in both *aft* and *gme* cages during hydrothermal aging may also lend an additional stabilization effect to framework structure. Furthermore, the hydrothermal treatment leads to the migration and re-distribution of $Cu^{2+}$-$^-$Z2 (or $Cu(OH)^+$-Z), which may induce the formation of $Cu(OH)^+$ sites neighboring with proton sites, the active sites that are more efficient than isolated $Cu^{2+}$-$^-$Z2 (or $Cu(OH)^+$-$^-$Z) sites [82]. The enhanced framework stability of the host **AFX** zeolite assists to maintain the active structure, which explains the observed high activity in the high temperature regime.

## 4. Conclusions

The increase of framework Si/Al ratio to 7.8 for **AFX** zeolite has been attained by the judicious choice of a rigid, high $C/N^+$ ratio (10) PD as OSDA and inexpensive **FAU** zeolite (Si/Al of 2.8 and 5.5) as Al source. By using **FAU** zeolites as aluminum source, together with the adoption of low alkali conditions, the synthetic yields for **AFX** zeolite have been increased. The successful synthesis can be ascribed to the low charge density of OSDA that stabilizes the *aft* cage and charge balances Si-rich framework. In addition, **FAU** precursor depolymerization releases *d6r* units and provides the building blocks that facilitates the formation of *d6r* prisms in the **AFX** framework. The hydrothermal stability for the generated Si-rich **AFX** zeolite has been markedly enhanced to an extent to withstand harsh hydrothermal treating at 850 °C for up to 10 h, owing to the formation of less numbers of thermally susceptible paired Al sites.

The ion-exchanged $Cu^{2+}$-type $NH_3$-SCR catalyst derived from the material comprises of predominantly $Cu(OH)^+$-$^-$Z sites that are situated co-cage within one *aft* cavity, therefore, facilitating the formation of key copper-dimer intermediates (a kinetically important step) and endowing a high low-temperature activity. The catalytic performance for the Si-rich catalyst after hydrothermal aging is comparable to that of the fresh catalysts for two reasons. First, the increase of framework Si/Al ratio endows a high hydrothermal stability, resulting from high crystallinity and less concentrations of vulnerable pair Al sites. Second, $Cu^{2+}$ cation re-distribution upon hydrothermal treating assists its migration to 6-MR, which exerts a further stabilization effect of framework and may assist the formation of more reactive $Cu^{2+}$ sites neighbored with protons. Both factors assist to broadened active temperature window.

The synthetic strategy is transferrable and the generation of Si-rich

**AFX** zeolite may promote its catalytic application in $NH_3$-SCR and alike reactions.

## Author statement

**Zheru Shi**: Synthesis, characterizations, data curation, wrote-original draft. **Han Sun**: Performed catalytic assessments and analysis. **Lei Wang**: Supervised analytical zeolite structure and refinement. **Quanzheng Deng** and **Lu Han**: Performed FE-SEM micrographs analysis. **Chen-Xin Gong** and **Yi-An Zhu**: Molecular mode calculation. **Kaixiang Li**: Carried out catalytic preparation and analysis. **Wei Deng**: Performed XPS measurement and analysis. **Zhenguo Li**: Supervised and assisted characterizations, **Haijun Chen**: Supervised the catalytic assessments studies, resources, writing-review & editing, **Kake Zhu**: Supervised and designed the research plan, funding acquisition, project administration, writing-review & editing.

## CRediT authorship contribution statement

**Li Zhengguo:** Funding acquisition, Resources, Supervision. **Zhu Kake:** Conceptualization, Funding acquisition, Investigation, Project administration, Resources, Supervision, Validation, Writing – review & editing. **Chen Haijun:** Funding acquisition, Project administration, Resources, Supervision. **Shi Zheru:** Conceptualization, Data curation, Formal analysis, Investigation, Methodology, Validation, Visualization, Writing – original draft, Writing – review & editing. **Sun Han:** Data curation, Formal analysis, Funding acquisition, Investigation, Methodology, Resources. **Wang Lei:** Data curation, Funding acquisition, Methodology, Resources, Software, Validation, Visualization. **Deng Quanzheng:** Data curation, Validation, Visualization. **Gong Chenxin:** Methodology, Software, Visualization. **Han Lu:** Validation, Visualization. **Li Kaixiang:** Data curation. **Deng Wei:** Methodology. **Zhu Yian:** Software, Supervision.

## Declaration of Competing Interest

We declare that we do not have any commercial or associative interest that represents a conflict of interest in connection with the work submitted.

## Data Availability

Data will be made available on request.

## Acknowledgements

KZ is grateful for the financial support from National Natural Science Foundation of China (21878079). LW is grateful for the Natural Science Foundation of China (No. 22008108), the Natural Science Foundation of Jiangsu Province (No. BK20200681); the Jiangsu Shuangchuang Project (No. 30547(2020)), the Nanjing Tech University Startup Foundation (No. 39837152). HC is grateful for the financial support from National Natural Science Foundation of China (22076081). HS is grateful for the Postdoctoral Science Foundation of China (2022M721704). ZL is grateful for the National key Research and Development Program of China (2022YFC3701803). The authors grateful for the catalytic characterization from National Engineering Laboratory for Mobile Source Emission Control Technology (NELMS2019A11). We thank the Shanghai Synchrotron Radiation Facility (SSRF, project No. 2020-SSRF-PT-013074) on an X-ray diffraction beamline (BL14B1). The authors thank Research Centre of Analysis and Test of East China University of Science and Technology for the help on the characterizations.

## Appendix A. Supporting information

Supplementary data associated with this article can be found in the online version at doi:10.1016/j.apcatb.2023.123637.

## References

[1] R. Burch, J.P. Breen, F.C. Meunier, A review of the selective reduction of NOx, with hydrocarbons under lean-burn conditions with non-zeolitic oxide and platinum group metal catalysts, Appl. Catal. B: Environ. 39 (2002) 283–303.
[2] X. Ye, J.E. Schmidt, R.P. Wang, I.K. van Ravenhorst, R. Oord, T. Chen, F. de Groot, F. Meirer, B.M. Weckhuysen, Deactivation of Cu-exchanged automotive-Emission $NH_3$-SCR catalysts elucidated with nanoscale resolution using scanning transmission X-ray microscopy, Angew. Chem., Int. Ed. 59 (2020) 15610–15617.
[3] M. Iwamoto, H. Furukawa, Y. Mine, F. Uemura, S.I. Mikuriya, S. Kagawa, Copper (Ii) ion-exchanged ZSM-5 zeolites as highly-active catalysts for direct and continuous decomposition of nitrogen monoxide, J. Chem. Soc., Chem. Commun. (16) (1986) 1272–1273.
[4] A. Corma, V. Fornés, E. Palomares, Selective catalytic reduction of $NO_x$ on Cu-beta zeolites, Appl. Catal. B: Environ. 11 (1997) 233–242.
[5] C. Liu, H. Wang, Z. Zhang, Q. Liu, The latest research progress of $NH_3$-SCR in the $SO_2$ resistance of the catalyst in low temperatures for selective catalytic reduction of $NO_x$, Catalysts 10 (2020) 1034–1052.
[6] Y.L. Shan, J.P. Du, Y. Zhang, W.P. Shan, X.Y. Shi, Y.B. Yu, R.D. Zhang, X.J. Meng, F. S. Xiao, H. He, Selective catalytic reduction of $NO_x$ with $NH_3$: opportunities and challenges of Cu-based small-pore zeolites, Natl. Sci. Rev. 8 (2021), nwab010.
[7] E. Borfecchia, P. Beato, S. Svelle, U. Olsbye, C. Lamberti, S. Bordiga, Cu-CHA-a model system for applied selective redox catalysis, Chem. Soc. Rev. 47 (2018) 8097–8133.
[8] A.M. Beale, F. Gao, I. Lezcano-Gonzalez, C.H.F. Peden, J. Szanyi, Recent advances in automotive catalysis for $NO_x$ emission control by small-pore microporous materials, Chem. Soc. Rev. 44 (2015) 7371–7405.
[9] T. Sonoda, T. Maruo, Y. Yamasaki, N. Tsunoji, Y. Takamitsu, M. Sadakane, T. Sano, Synthesis of high-silica AEI zeolites with enhanced thermal stability by hydrothermal conversion of FAU zeolites, and their activity in the selective catalytic reduction of $NO_x$ with $NH_3$, J. Mater. Chem. A. 3 (2015) 857–865.
[10] M. Moliner, C. Franch, E. Palomares, M. Grill, A. Corma, Cu-SSZ-39, an active and hydrothermally stable catalyst for the selective catalytic reduction of $NO_x$, Chem. Commun. 48 (2012) 8264–8266.
[11] A. Hoffmann, M. De Prins, S.P. Sree, G. Vanbutsele, S. Smet, C.V. Chandran, S. Radhakrishnan, E. Breynaert, J.A. Martens, Selective catalytic reduction of $NO_{(x)}$ with ammonia ($NH_3$-SCR) over copper loaded LEV type zeolites synthesized with different templates, Phys. Chem. Chem. Phys. 24 (2022) 15428–15438.
[12] L.H. Shi, V. Vivek, D. Yu, M.M. Wei, H.T. Liu, L. Jin, Synthesis of zeolite materials having AFT framework structure and SCR catalysts comprising the same, WO2022199574A, 2022.
[13] J. Zhu, Z. Liu, L. Xu, T. Ohnishi, Y. Yanaba, M. Ogura, T. Wakihara, T. Okubo, Understanding the high hydrothermal stability and $NH_3$-SCR activity of the fast-synthesized ERI zeolite, J. Catal. 391 (2020) 346–356.
[14] D. Jo, T. Ryu, G.T. Park, P.S. Kim, C.H. Kim, I.S. Nam, S.B. Hong, Synthesis of High-Silica LTA and UFI Zeolites and $NH_3$-SCR performance of their Copper-exchanged form, ACS Catal. 6 (2016) 2443–2447.
[15] T. Ryu, N.H. Ahn, S. Seo, J. Cho, H. Kim, D. Jo, G.T. Park, P.S. Kim, C.H. Kim, E. L. Bruce, P.A. Wright, I.S. Nam, S.B. Hong, Fully copper-exchanged High-Silica LTA Zeolites as unrivaled hydrothermally stable $NH_3$-SCR catalysts, Angew. Chem., Int. Ed. 56 (2017) 3256–3260.
[16] J. Kim, S.J. Cho, D.H. Kim, Facile synthesis of KFI-type zeolite and Its application to selective catalytic reduction of $NO_x$ with $NH_3$, ACS Catal. 7 (2017) 6070–6081.
[17] J.D. Albarracin-Caballero, I. Khurana, J.R. Di Iorio, A.J. Shih, J.E. Schmidt, M. Dusselier, M.E. Davis, A. Yezerets, J.T. Miller, F.H. Ribeiro, R. Gounder, Structural and kinetic changes to small-pore Cu-zeolites after hydrothermal aging treatments and selective catalytic reduction of $NO_x$ with ammonia, React. Chem. Eng. 2 (2017) 168–179.
[18] D. Jo, J.B. Lim, T. Ryu, I.-S. Nam, M.A. Camblor, S.B. Hong, Unseeded hydroxide-mediated synthesis and $CO_2$ adsorption properties of an aluminosilicate zeolite with the RTH topology, J. Mater. Chem. A 3 (2015) 19322–19329.
[19] R. Li, Y. Zhu, Z. Zhang, C. Zhang, G. Fu, X. Yi, Q. Huang, F. Yang, W. Liang, A. Zheng, J. Jiang, Remarkable performance of selective catalytic reduction of NOx by ammonia over copper-exchanged SSZ-52 catalysts, Appl. Catal. B: Environ. 283 (2021) 119641–119651.
[20] D. Xie, L.B. McCusker, C. Baerlocher, S.I. Zones, W. Wan, X. Zou, SSZ-52, a zeolite with an 18-layer aluminosilicate framework structure related to that of the $DeNO_x$ catalyst Cu-SSZ-13, J. Am. Chem. Soc. 135 (2013) 10519–10524.
[21] N. Martín, C. Paris, P.N.R. Vennestrøm, J.R. Thøgersen, M. Moliner, A. Corma, Cage-based small-pore catalysts for $NH_3$-SCR prepared by combining bulky organic structure directing agents with modified zeolites as reagents, Appl. Catal. B: Environ. 217 (2017) 125–136.
[22] A. Guo, H. Liu, Y. Li, Y. Luo, Da Ye, J. Jiang, P. Chen, Recent progress in novel zeolite catalysts for selective catalytic reduction of nitrogen oxides, Catal. Today 422 (2023) 114212–114232.
[23] A. Chokkalingam, W. Chaikittisilp, K. Iyoki, S.H. Keoh, Y. Yanaba, T. Yoshikawa, T. Kusamoto, T. Okubo, T. Wakihara, Ultrafast synthesis of AFX-Type zeolite with enhanced activity in the selective catalytic reduction of $NO_x$ and hydrothermal stability, RSC Adv. 9 (2019) 16790–16796.
[24] M. Dusselier, M.E. Davis, Small-Pore Zeolites: Synthesis and Catalysis, Chem. Rev. 118 (2018) 5265–5329.
[25] R.F. Lobo, Synthesis and Rietveld Refinement of the Small-Pore Zeolite SSZ-16, Chem. Mater. 8 (1996) 2409–2411.

[26] S.I. Zones, Zeolite SSZ-16, US4508837, 1985.
[27] M. Onishi, N. Tsunoji, M. Sadakane, T. Sano, Synthesis of phosphorus-modified AFX zeolite by the hydrothermal conversion of tetraalkylphosphonium hydroxide-impregnated FAU zeolite, Bull. Chem. Soc. Jpn. 94 (2021) 1–7.
[28] P. Hrabanek, A. Zikanova, T. Supinkova, J. Drahokoupil, V. Fila, M. Lhotka, H. Dragounova, F. Laufek, L. Brabec, I. Jirka, B. Bernauer, O. Prokopova, V. Martin-Gil, M. Kocirik, Static in-situ hydrothermal synthesis of small pore zeolite SSZ-16 (AFX) using heated and pre-aged synthesis mixtures, Micro Mesopor. Mater. 228 (2016) 107–115.
[29] S. Han, W. Rao, J. Hu, X. Tang, Y. Ma, J. Du, Z. Liu, Q. Wu, Y. Ma, X. Meng, W. Shan, F.S. Xiao, H. He, Direct synthesis of high silica SSZ-16 zeolite with extraordinarily superior performance in $NH_3$-SCR reaction, Appl. Catal. B: Environ. 332 (2023), 122746-12254.
[30] Y. Bhawe, M. Moliner-Marin, J.D. Lunn, Y. Liu, A. Malek, M. Davis, Effect of Cage Size on the Selective Conversion of Methanol to Light Olefins, ACS Catal. 2 (2012) 2490–2495.
[31] N. Nakazawa, S. Inagaki, Y. Kubota, Novel Technique to Synthesize AFX-Type Zeolite Using a Bulky and Rigid Diquaternary Ammonium Cation, Adv. Porous Mater. 4 (2016) 219–229.
[32] N. Tsunoji, K. Tsuchiya, N. Nakazawa, S. Inagaki, Y. Kubota, T. Nishitoba, T. Yokoi, T. Ohnishi, M. Ogura, M. Sadakane, T. Sano, Multiple templating strategy for the control of aluminum and phosphorus distributions in AFX zeolite, Micro Mesopor. Mater. 321 (2021) 111124–111134.
[33] F. Gao, D. Mei, Y. Wang, J. Szanyi, C.H. Peden, Selective Catalytic reduction over Cu/SSZ-13: Linking Homo- and Heterogeneous Catalysis, J. Am. Chem. Soc. 139 (2017) 4935–4942.
[34] C. Paolucci, A.A. Parekh, I. Khurana, J.R. Di Iorio, H. Li, J.D. Albarracin Caballero, A.J. Shih, T. Anggara, W.N. Delgass, J.T. Miller, F.H. Ribeiro, R. Gounder, W. F. Schneider, Catalysis in a Cage: Condition-Dependent Speciation and Dynamics of Exchanged Cu Cations in SSZ-13 Zeolites, J. Am. Chem. Soc. 138 (2016) 6028–6048.
[35] J. Lin, X. Hu, Y. Li, W. Shan, X. Tan, H. He, Maximizing the hydrothermal stability of Cu-LTA for $NH_3$-SCR by control of Cu content and location, Appl. Catal. B: Environ. 331 (2023) 122705–122715.
[36] H. Wang, R. Xu, Y. Jin, R. Zhang, Zeolite structure effects on Cu active center, SCR performance and stability of Cu-zeolite catalysts, Catal. Today 327 (2019) 295–307.
[37] K.A. Tarach, M. Jabłońska, K. Pyra, M. Liebau, B. Reiprich, R. Gläser, K. Góra-Marek, Effect of zeolite topology on $NH_3$-SCR activity and stability of Cu-exchanged zeolites, Appl. Catal. B: Environ. 284 (2021) 119752–119768.
[38] Q. Guo, F. Fan, D.A.J.M. Ligthart, G. Li, Z. Feng, E.J.M. Hensen, C. Li, Effect of the nature and location of copper species on the catalytic nitric oxide selective catalytic reduction performance of the copper/SSZ-13 Zeolite, ChemCatChem 6 (2014) 634–639.
[39] Y. Shan, X. Shi, G. He, K. Liu, Z. Yan, Y. Yu, H. He, Effects of $NO_2$ addition on the $NH_3$-SCR over small-pore Cu–SSZ-13 zeolites with varying cu loadings, J. Phys. Chem. C. 122 (2018) 25948–25953.
[40] M.A. Deimund, L. Harrison, J.D. Lunn, Y. Liu, A. Malek, R. Shayib, M.E. Davis, Effect of heteroatom concentration in SSZ-13 on the methanol-to-olefins reaction, ACS Catal. 6 (2016) 542–550.
[41] Y. Shan, Y. Sun, J. Du, Y. Zhang, X. Shi, Y. Yu, W. Shan, H. He, Hydrothermal aging alleviates the inhibition effects of $NO_2$ on Cu-SSZ-13 for $NH_3$-SCR, Appl. Catal. B: Environ. 275 (2020) 119105–119115.
[42] S.I. Zones, Conversion of faujasites to high-silica chabazite SSZ-13 in the presence of N,N,N-Trimethyl-l -adamantammonium Iodide, J. Chem. Soc. Faraday Trans. 87 (1991) 3709–3716.
[43] N.H. Ahn, T. Ryu, Y. Kang, H. Kim, J. Shin, I.S. Nam, S.B. Hong, The Origin of an Unexpected Increase in $NH_3$-SCR Activity of Aged Cu-LTA Catalysts, ACS Catal. 7 (2017) 6781–6785.
[44] R.F. Lobo, S.I. Zones, M.E. Davis, Structure-Direction in Zeolite Synthesis, J. Incl. Phenom. 21 (1995) 47–78.
[45] Y. Kubota, M.M. Helmkamp, S.I. Zones, M.E. Davis, Properties of organic cations that lead to the structure-direction of high-silica molecular sieves, Micro Mater. 6 (1996) 213–229.
[46] G.J. Lewis, M.A. Miller, J.G. Moscoso, B.A. Wilson, L.M, S.T. Wilson, Experimental charge density matching approach to zeolite synthesis, Stud. Surf. Sci. Catal. 154 (2004) 364–372.
[47] C.S. Blackwell, R.W. Broach, M.G. Gatter, J.S. Holmgren, D.Y. Jan, G.J. Lewis, B. J. Mezza, T.M. Mezza, M.A. Miller, J.G. Moscoso, R.L. Patton, L.M. Rohde, M. W. Schoonover, W. Sinkler, B.A. Wilson, S.T. Wilson, Open-framework materials synthesized in the $TMA^+/TEA^+$ mixed-template system: the new low Si/Al ratio zeolites UZM-4 and UZM-5, Angew. Chem. Int. Ed. 42 (2003) 1737–1740.
[48] S.A. Bates, A.A. Verma, C. Paolucci, A.A. Parekh, T. Anggara, A. Yezerets, W. F. Schneider, J.T. Miller, W.N. Delgass, F.H. Ribeiro, Identification of the active Cu site in standard selective catalytic reduction with ammonia on Cu-SSZ-13, J. Catal. 312 (2014) 87–97.
[49] Z.G. Li, Z.R. Shi, K.K. Zhu, X.N. Ren, K.X. Li, Y.K. Shao, H.M. Wu, Structure directing agent containing quaternary ammonium salt or a base, its preparation method and application, CN112939021B (2021).
[50] S.I. Zones, S. Francisco, Synthesis of SSZ-16 zeolite catalyst, US5194235A, 1993.
[51] F. Dogan, K.D. Hammond, G.A. Tompsett, H. Huo, W.C. Conner Jr., S.M. Auerbach, C.P. Grey, Searching for microporous, strongly basic catalysts: experimental and calculated $^{29}Si$ NMR spectra of heavilynitrogen-doped Y, Zeolites, J. Am. Chem. Soc. 131 (2009) 11062–11079.
[52] T. Barzetti, E. Selli, D. Moscotti, L. Forni, Pyridine and ammonia as probes for FTIR analysis of solid acid catalysts, J. Chem. Soc., Faraday Trans. 92 (1996) 1401–1407.
[53] J. Li, A. Corma, J. Yu, Synthesis of new zeolite structures, Chem. Soc. Rev. 44 (2015) 7112–7127.
[54] M. Moliner, F. Rey, A. Corma, Towards the rational design of efficient organic structure-directing agents for zeolite synthesis, Angew. Chem. Int. Ed. 52 (2013) 13880–13889.
[55] M.L. Occelli, H. Kessler, Synthesis of Porous Materials: Zeolites, Clays and Nanostructures, Marcel Dekker,, New York, 1996, pp. 1–34.
[56] M. Itakura, T. Inoue, A. Takahashi, T. Fujitani, Y. Oumi, T. Sano, Synthesis of High-silica CHA Zeolite from FAU Zeolite in the Presence of Benzyltrimethylammonium Hydroxide, Chem. Lett. 37 (2008) 908–909.
[57] C.-R. Boruntea, L.F. Lundegaard, A. Corma, P.N.R. Vennestrøm, Crystallization of AEI and AFX zeolites through zeolite-to-zeolite transformations, Micro Mesopor. Mater. 278 (2019) 105–114.
[58] T. Maruo, N. Yamanaka, N. Tsunoji, M. Sadakane, T. Sano, Facile synthesis of AEI zeolites by hydrothermal conversion of fau zeolites in the presence of tetraethylphosphonium cations, Chem. Lett. 43 (2014) 302–304.
[59] R. Jain, Z. Niu, M. Choudhary, H. Bourji, J.C. Palmer, J.D. Rimer, In situ imaging of faujasite surface growth reveals unique pathways of zeolite crystallization, J. Am. Chem. Soc. 145 (2023) 1155–1164.
[60] W.H. Baur, R.X. Fischer, The floppiness of It all: bond lengths change with atomic displacement parameters and the flexibility of various coordination tetrahedra in zeolitic frameworks. An Empirical Structural Study of Bond Lengths and Angles, Chem. Mater. 31 (2019) 2401–2420.
[61] J.F. Moulder, W.F. Stickle, P.E. Sobol, K. D.bomben, Handbook of X-ray Photoelectron Spectroscopy, Perkin-Elmer Corporation Physical Electronics Division, 6509 Flying Cloud Drive, Eden Prairie, Minnesota 55344, USA (1992) 45.
[62] J.H. Kwak, H. Zhu, J.H. Lee, C.H.F. Peden, J. Szanyi, Two different cationic positions in Cu-SSZ-13, Chem. Commun. 48 (2012) 4758–4760.
[63] D.W. Fickel, R.F. Lobo, Copper coordination in Cu-SSZ-13 and Cu-SSZ-16 investigated by Variable-Temperature XRD, J. Phys. Chem. C. 114 (2010) 1633–1640.
[64] Y.L. Shan, J.P. Du, Y.B. Yu, W.P. Shan, X.Y. Shi, H. He, Precise control of post-treatment significantly increases hydrothermal stability of in-situ synthesized cu-zeolites for $NH_3$-SCR reaction, Appl. Catal. B: Environ. 266 (2020), 118655.
[65] D. Wang, L. Zhang, K. Kamasamudram, W.S. Epling, In Situ-DRIFTS study of selective catalytic reduction of $NO_x$ by $NH_3$ over Cu-exchanged SAPO-34, ACS Catal. 3 (2013) 871–881.
[66] J. Szanyi, J.H. Kwak, H.Y. Zhu, C.H.F. Peden, Characterization of Cu-SSZ-13 $NH_3$-SCR catalysts: an in situ FTIR study, Phys. Chem. Chem. Phys. 15 (2013) 2368–2380.
[67] T. Nanba, S. Masukawa, A. Ogata, J. Uchisawa, A. Obuchi, Active sites of Cu-ZSM-5 for the decomposition of acrylonitrile, Appl. Catal. B: Environ. 61 (2005) 288–296.
[68] F. Gao, Y. Wang, N.M. Washton, M. Kollár, J. Szanyi, C.H.F. Peden, Effects of Alkali and Alkaline Earth Cocations on the Activity and Hydrothermal Stability of Cu/SSZ-13 $NH_3$–SCR Catalysts, ACS Catal. 5 (2015) 6780–6791.
[69] A.V. Kucherov, A.N. Shigapov, A.A. Ivanov, M. Shelef, Stability of the Square-Planar $Cu^{2+}$ Sites in ZSM-5: Effect of preparation, heat treatment, and modification, J. Catal. 186 (1999) 334–344.
[70] H. Kubota, C. Liu, T. Toyao, Z. Maeno, M. Ogura, N. Nakazawa, S. Inagaki, Y. Kubota, K.-i Shimizu, Formation and reactions of $NH_4NO_3$ during transient and steady-state $NH_3$-SCR of $NO_x$ over H-AFX zeolites: spectroscopic and theoretical studies, ACS Catal. 10 (2020) 2334–2344.
[71] D.W. Fickel, E. D'Addio, J.A. Lauterbach, R.F. Lobo, The ammonia selective catalytic reduction activity of copper-exchanged small-pore zeolites, Appl. Catal. B: Environ. 102 (2011) 441–448.
[72] J. Eng, C.H. Bartholomew, Kinetic and mechanistic study of $NO_x$ Reduction by $NH_3$ over H-Form zeolites II. semi-steady-state and in situ FTIR studies, J. Catal. 171 (1997) 27–44.
[73] B. Chen, J. Cheng, J. Qiao, C. Dai, R. Xu, G. Yu, N. Wang, J. Xing, N. Liu, Understanding of low- and high-temperature $DeNO_x$ efficiency for $NH_3$-SCR via comparison on Cu modified CHA and AFX zeolites, Fuel 348 (2023) 128501–128513.
[74] S.J. Schmieg, S.H. Oh, C.H. Kim, D.B. Brown, J.H. Lee, C.H.F. Peden, D.H. Kim, Thermal durability of Cu-CHA $NH_3$-SCR catalysts for diesel NO reduction, Catal. Today 184 (2012) 252–261.
[75] C. Paolucci, I. Khurana, A.A. Parekh, S.C. Li, A.J. Shih, H. Li, J.R. Di Iorio, J. D. Albarracin-Caballero, A. Yezerets, J.T. Miller, W.N. Delgass, F.H. Ribeiro, W. F. Schneider, R. Gounder, Dynamic multinuclear sites formed by mobilized copper ions in $NO_x$ selective catalytic reduction, Science 357 (2017) 898–903.
[76] Y. Wu, W. Zhao, S.H. Ahn, Y. Wang, E.D. Walter, Y. Chen, M.A. Derewinski, N. M. Washton, K.G. Rappé, Y. Wang, D. Mei, S.B. Hong, F. Gao, Interplay between copper redox and transfer and support acidity and topology in low temperature $NH_3$-SCR, Nat. Commun. 14 (2023) 2633–2636.
[77] W. Hu, T. Selleri, F. Gramigni, E. Fenes, K.R. Rout, S. Liu, I. Nova, D. Chen, X. Gao, E. Tronconi, On the redox mechanism of low-temperature $NH_3$-SCR over Cu-CHA: a combined experimentaland theoretical study of the reduction half cycle, Angew. Chem., Int. Ed. 60 (2021) 7197–7204.
[78] C. Liu, H. Kubota, T. Amada, T. Toyao, Z. Maeno, M. Ogura, N. Nakazawa, S. Inagaki, Y. Kubota, Shimizu K.-i, Selective catalytic reduction of NO over Cu-AFX zeolites: mechanistic insights from in situ/operando spectroscopic and DFT studies, Catal. Sci. Technol. 11 (2021) 4459–4470.

[79] C. Fan, Z. Chen, L. Pang, S.J. Ming, X.F. Zhang, K.B. Albert, P. Liu, H.P. Chen, T. Li, The influence of Si/Al ratio on the catalytic property and hydrothermal stability of Cu-SSZ-13 catalysts for $NH_3$-SCR, Appl. Catal. A: Gen. 550 (2018) 256–265.
[80] J. Song, Y.L. Wang, E.D. Walter, N.M. Washton, D.H. Mei, L. Kovarik, M. H. Engelhard, S. Prodinger, Y. Wang, C.H.F. Penden, F. Gao, Toward rational design of Cu/SSZ-13 selective catalytic reduction catalysts: implications from atomic-level understanding of hydrothermal stability, ACS Catal. 7 (2017) 8214–8227.
[81] F. Gao, E.D. Walter, M. Kollar, Y. Wang, J. Szanyi, C.H.F. Peden, Understanding ammonia selective catalytic reduction kinetics over Cu/SSZ-13 from motion of the Cu ions, J. Catal. 319 (2014) 1–14.
[82] C. Paolucci, A.A. Verma, S.A. Bates, V.F. Kispersky, J.T. Miller, R. Gounder, W. N. Delgass, F.H. Ribeiro, W.F. Schneider, Isolation of the copper redox steps in the standard selective catalytic reduction on Cu-SSZ-13, Angew. Chem., Int. Ed. 53 (2014) 11828–11833.